IIETA International Information and Engineering Technology Association
Advancing the World of Information and Engineering

Journal Européen des Systèmes Automatisés
Vol. 58, No. 11, November, 2025, pp. 2351-2366
Journal homepage: http://iieta.org/journals/jesa

Multi-Criteria Evaluation of MPPT Algorithms under Time-Varying Partial Shading Using a Physics-Based PV Model

Minh-Cuong Nguyen[1,2]

[1] Education Technology and Adaptive Learning Institute, Thai Nguyen University of Technology, Thai Nguyen 24000, Vietnam
[2] Faculty of Electrical Engineering, Thai Nguyen University of Technology, Thai Nguyen 24000, Vietnam

Corresponding Author Email: nmc.etali@tnut.edu.vn

https://doi.org/10.18280/jesa.581113

Received: 17 October 2025
Revised: 21 November 2025
Accepted: 25 November 2025
Available online: 30 November 2025

Keywords:
partial shading, maximum power point tracking, photovoltaic, global MPP, multicriteria evaluation

ABSTRACT

This work investigates how widely used MPPT algorithms perform under realistic, time-varying partial shading and aims to provide an objective, reproducible basis for multicriteria decision-making. We implement a 60cell module model (three substrings with bypass diodes) driven by a 10s mixed shading profile at 1ms resolution; an internal oracle computes the instantaneous global MPP solely for scoring. Performance is quantified by oracle-normalized energy, a formally defined time-to-sustain t_{95}, GMPP hit/dwell ratio, and a ripple/PRI; distributional behavior (histograms/CDF/boxplots), nonparametric inference (Kruskal–Wallis, Cliff's δ), bootstrap confidence intervals, and a weight-transparent composite score (0.30 energy, 0.25 hit, 0.25 speed, 0.20 ripple) complement the analysis, with sensitivity/ablation on step sizes, swarm settings, attractiveness/Lévy steps, and weights. Incremental Conductance achieves the highest energy (0.281 Wh), fast convergence (t_{95} = 3.0 ms), the best hit ratio (62.8%), and the lowest ripple (41.4 W). PSO yields intermediate energy (0.231 Wh) but long convergence (206.2 ms), FP responds fastest (t_{95} = 2.6 ms) yet records the lowest energy (0.094 Wh) and hit ratio (10.8%), and P&O is simple but ripple-prone (100.1 W) with lower energy (0.143 Wh). Despite universal large transient errors during regime changes (~220 W), distributional evidence and robustness checks consistently favor Incremental Conductance. The framework and metric suite offer reusable guidance for algorithm selection under partial shading and clarify when exploration latency or instability erodes net yield.

1. INTRODUCTION

Partial shading (PSC) creates spatially nonuniform irradiance across series-connected substrings in a photovoltaic (PV) module, forcing bypass diodes to conduct and producing multipeak P–V characteristics with multiple local maxima. The resulting mismatch losses depress array energy yield and complicate real-time control, as a tracker can settle on a suboptimal local MPP when the global MPP (GMPP) shifts with irradiance and temperature transients [1]. Hardware choices such as bypass-diode count and placement shape the piecewise I–V/P–V landscape and the severity of local-peak trapping, further entangling the control problem under PSC [2]. These effects motivate MPPT strategies that are simultaneously fast, accurate, and robust to rapidly evolving operating points while remaining compatible with embedded constraints on sensing, computation, and voltage/current limits [3, 4].

The literature reflects two complementary avenues to tackle PSC. The first is converter/architecture co-design that mitigates mismatch at the source or augments controllability; the second is algorithmic MPPT that can search for and track the GMPP on a multi-modal surface in real time. On the converter side, string- and module-level innovations, from active array structures and multi-input converters to equalization and differential-power-processing (DPP) modules, aim to decouple shaded elements and reduce the formation or impact of local peaks [3]. Yet, even with architectural assistance, robust GMPP tracking remains necessary because PSC dynamics (e.g., cloud-edge events) move the optimum faster than slow or purely local controllers can track [4].

Algorithmically, recent work spans classical hill-climbing and a broad family of metaheuristics tailored for multi-peak search. Hybrid and predictive designs improve the global search–local tracking balance: for example, a modified PSO combined with model predictive control accelerates transients and raises steady-state efficiency under PSC [5]. Adaptive single-solution schemes such as Ajaya reduce settling time and curtail oscillations, targeting low-cost controllers without sacrificing robustness [6], while hybrid evolutionary designs (e.g., PSO+DE) improve reliability in escaping local peaks and locating the true GMPP in hardware-validated tests [7]. Algorithm selection continues to trade off exploration latency, parameter tuning effort, and ripple around the operating point, particularly in fast transients where excessive global search

can undercut net energy capture [8].

Beyond PSO-like families, multi-producer group-search optimization and other swarm/animal-inspired strategies have been proposed to avoid local optimum lock-in and raise utilization under both uniform and PSC conditions [9]. Likewise, refinements to bat- and mayfly-based trackers report higher tracking accuracy and shorter dynamic response by embedding explicit shading detection or hybridized update rules, further illustrating the field's shift toward condition-aware global tracking under PSC [10, 11]. Collectively, these advances underline the central control challenge: to sustain high energy harvest while minimizing convergence time and output ripple, despite the nonconvex and time-varying P–V landscape that PSC generates.

In parallel, architecture-level mismatch mitigation has matured. Submodule-level DPP with local MPPT can substantially suppress mismatch losses by processing only the differential power, improving efficiency relative to module optimizers and diode-only strategies [12]. Modular switched-capacitor DPP architectures generalize to longer strings and enable scalable deployment without bespoke converter redesigns, extending the operating envelope under PSC [13]. Segmented and distributed-control DPP schemes further reduce processed power and improve resilience in harsh mismatch scenarios, with both simulation and hardware validation supporting efficiency gains [14-16]. Such approaches narrow the gap between local and global MPPs but do not obviate the need for fast, accurate MPPT when irradiance varies quickly across substrings.

Complementary to DPP, voltage equalizers (VEs) and equalizer-aware topologies can preempt bypass-diode conduction, reduce the creation of deep secondary peaks and improve the effective search landscape for MPPT. Recent comparative quantization establishes practical selection guidelines among VE families, relating topology to mismatch severity and dynamic response [17]. Equalizers that are extendable with reduced switch count demonstrate large energy-yield improvements and quick tracking, indicating that topology can materially ease the control burden under PSC [18]. At the array level, active PV (APV) structures show substantial power enhancements under non-uniform conditions, again emphasizing that architecture and control co-design is a promising path to holistic robustness [19].

Array-level reconfiguration provides yet another lever: rearranging interconnections to spread shading and equalize substring currents can flatten the multi-peak structure and raise output power, especially in persistent shading patterns [20]. Heuristic and optimization-guided layouts (and their fast online surrogates) redistribute mismatch to reduce the most pathological local peaks and improve the operating margin for MPPT [21, 22]. Still, reconfiguration rarely eliminates PSC dynamics; trackers must continue to locate and follow the instantaneous GMPP as conditions evolve.

Taken together, the problem statement is clear. PSC induces multi-peak P–V surfaces and rapid operating-point migration; neither bypass diodes nor architectural remedies alone guarantee high-yield operation when irradiance is time-varying. Robust MPPT must therefore (i) converge rapidly to the GMPP after irradiance/temperature perturbations, (ii) sustain high steady-state accuracy with low ripple to preserve power quality, and (iii) integrate cleanly with modern converter/DPP/VE/APV hardware across a full operating range. State-of-the-art GMPPT designs explicitly target rapid PSC, reporting the fastest and most reliable responses in comparative tests, yet they also highlight sensitivity to exploration latency and implementation overheads [23]. Meanwhile, partial-power processing and module-integrated converters extend the full-range MPPT envelope with high conversion efficiency, but still rely on the MPPT layer to resolve global from local peaks under mismatch [24, 25].

Despite steady progress on global MPPT under PSC, most recent studies still report algorithm-centric wins without a standardized, multi-criteria benchmark that jointly quantifies convergence (e.g., t_{95}), accuracy (GMPP hit/dwell behavior), and power quality: ripple/Power Ripple Index (PRI), alongside distributional statistics (loss and error distributions) and non-parametric significance tests. Typical exemplars demonstrate credible GMPPT improvements yet omit a common metric suite and robust statistical treatment, limiting cross-paper comparability and masking trade-offs across scenarios [26, 27]. Hybrid heuristics and enhanced RCC variants likewise emphasize faster search or higher instantaneous efficiency but rarely disclose GMPP dwell time, loss distributions, or formal ranking criteria applicable across shading dynamics and hardware budgets [28-30]. Even when dynamic response is reduced or accuracy exceeds 99%, studies often do not report standardized t_{95}, GMPP hit ratio definitions, or uncertainty quantification across runs and patterns [31, 32].

Data-driven and model-assisted trackers add speed and global awareness but still tend to publish point estimates (e.g., mean efficiency or settling time) without variance, effect size, or non-parametric tests suited to skewed error/loss distributions under PSC [33, 34]. Methods enabling flexible power tracking or capacitor-transient tracing further broaden functionality, yet comparative evaluation lacks harmonized metrics and composite scores that weight energy, speed, accuracy, and ripple in a transparent way [35-37]. Likewise, hybrid evolutionary approaches and empirical PSC characterizations enrich the design space but stop short of reproducible, multi-criteria ranking with sensitivity analysis to metric weights and scenario mix [38, 39]. Recent GFPPT and team-game variants report guaranteed and fast convergence, but do not provide GMPP dwell/hit statistics or distributional ripple/error analyses necessary to establish robustness across transients [40, 41].

Broader swarm families and systematic evaluations help normalize test procedures, yet either do not target PSC metrics explicitly or still omit non-parametric inference (e.g., Kruskal–Wallis, Cliff's delta) for non-Gaussian outcomes [42-44]. On the hardware side, equalizers, centralized farm controls, and restart conditions reduce search overheads but rarely integrate a common MPPT metric suite or composite ranking that spans controller and topology choices [45-47]. Converter-level advances (e.g., HMMC, model-based CPG with fast DC-link dynamics) expand the operating envelope but still depend on comparable, statistically sound MPPT reporting to claim robustness under realistic PSC [48, 49]. Finally, array-reconfiguration studies prioritize output improvements yet typically lack standardized definitions of t_{95}, GMPP dwell/hit, and loss distribution reporting tied to a reusable ranking framework [50]. These gaps motivate a reproducible benchmarking protocol that (i) defines t_{95}, GMPP hit/dwell, ripple/PRI, and loss/error distributions; (ii) applies non-parametric tests and effect sizes; and (iii) yields a transparent composite score with weight-sensitivity analysis for objective, cross-scenario ranking.

Building on the above gap analysis, prior art on MPPT under PSC clusters into classical gradient/perturbation

schemes, population-based metaheuristics, and bio-inspired/intelligent hybrids. Classical methods remain attractive for their simplicity and low computational cost, yet they are prone to oscillations and local-peak trapping when the *P-V* surface is multi-modal. Variable-perturbation P&O with PR–P compensation improves settling and reduces steady-state ripple, but it cannot fully neutralize local-maximum lock-in under aggressive PSC transients [51]. Comparative testing under EN50530 confirms that fixed-step P&O may drift and lag during rapid irradiance changes, while improved incremental/variable-step variants fare better but still expose trade-offs between speed and stability [52]. Geometry-aided refinements (e.g., CCC P&O) further cut iterations and oscillations, yet they inherit the same local-search limitation whenever multiple peaks persist [53].

Augmenting classical schemes with auxiliary estimation or adaptive tuning yields further gains. Particle-swarm-optimized step sizing for P&O/INC accelerates convergence without manual retuning [54], and combining simplified state estimation with adaptive P&O boosts > 99% tracking accuracy while shortening transient time substantially [55]. Learning-assisted variable-step controllers (e.g., ANN-based) likewise smooth oscillations and improve efficiency relative to baseline P&O/INC under PSC; however, they still require careful generalization checks across shading patterns and device noise [56].

Metaheuristic trackers target the global landscape directly. Hybrid PSO–DE schemes reliably escape local maxima and improve dynamic response in multi-peak profiles [57], while cuckoo-optimized fuzzy logic controllers report both efficiency gains and ripple reduction under diverse conditions [58]. Other swarms, Bat and Artificial Bee Colony, show strong global search and robustness to pattern shifts, but incur parameter-sensitivity and latency overheads that can erode net energy when PSC varies rapidly [59, 60]. At finer granularity, distributed MPPT with an improved sparrow-search controller enhances microgrid-level energy capture by mitigating mismatch locally, though at the cost of added coordination complexity [61]. Cross-domain evidence from wind-energy MPPT (SSM-PSO) reinforces these convergence/robustness benefits for population methods, while also highlighting their tuning burden under fast dynamics [62].

Within bio-inspired and recent hybrid lines, shade-aware hybrids that blend fast local P&O with Firefly-style global steps improve hit rates under PSC while containing ripple [63]. Rapid Jaya-family variants further reduce settling time and fluctuations, making them appealing for low-cost controllers, albeit still dependent on heuristic parameter bounds [64]. A recent survey synthesizes these trends, classical methods are hardware-friendly but locally myopic; metaheuristics are globally capable but compute- and tuning-intensive; hybrids trade complexity for better Pareto balance [65]. Newer reduced-search-space metaheuristics aim to keep global reach with lower computational burden [66], while controller-level advances, fuzzy-immune P&O with GA auto-tuning, and nonlinear PID combined with swarm optimization, push tracking speed/efficiency without excessive ripple [67, 68]. Finally, anti-windup ANN-based MPPT with robust PI clamping demonstrates strong performance under rapidly changing conditions, yet its benefits depend on training coverage and embedded implementation constraints [69]. In sum, under PSC: P&O/INC excel in simplicity and latency but risk local entrapment; PSO/GA/DE and cognate swarms improve globality at the expense of tuning and real-time compute; bio-inspired hybrids narrow the gap, provided their adaptation logic is paired with reproducible, scenario-aware evaluation.

Although a wide variety of maximum power point tracking (MPPT) strategies have been reported in the literature, this study deliberately focuses on four representative algorithms that span the main methodological families in current photovoltaic applications. The perturb-and-observe (P&O) and incremental conductance (INC) methods are selected as classical deterministic techniques, with P&O reflecting the simplest and most widely implemented industrial approach, while INC represents a gradient-based scheme with higher steady-state accuracy. Particle swarm optimisation (PSO) is included as a typical population-based metaheuristic, capable of global exploration in highly non-linear and multimodal power–voltage landscapes. In parallel, the flower pollination (FP) algorithm is considered as a representative bio-inspired method, characterised by Lévy-flight-based exploration and strong non-linear optimisation capability under partial shading conditions. Together, these four algorithms form a compact yet comprehensive spectrum encompassing the dominant paradigms in MPPT research, thereby enabling a structured and meaningful comparative evaluation under identical physical and environmental constraints.

Addressing the above gaps, this paper makes four contributions: first, it introduces a reproducible MPPT benchmarking framework, built on a physics-based 60-cell PV module (three substrings with bypass diodes) and a time-varying, parametric partial-shading generator, with an internal scan-plus-refine procedure to compute the instantaneous GMPP as ground truth and avoid evaluation bias; second, it defines a principled multi-criteria metric suite that quantifies cumulative energy (Wh), formally defined convergence time t_{95} (sustained within $\pm 5\%$ of steady power), GMPP hit ratio, and power-quality ripple/PRI, complemented by tracking-error and loss-distribution statistics, a stability index, and an interpretable improvement vector $\Delta = \{\Delta E, \Delta\text{Speed}, \Delta\text{Accuracy}, \Delta\text{Ripple}\}$, and aggregates them via a normalized composite score with transparent weights (0.30 energy, 0.25 hit ratio, 0.25 speed, 0.20 ripple) and sensitivity analysis; third, it delivers a comparative study of P&O, INC, PSO, and FP that expose dynamic trajectories, multi-peak operating regimes, robustness/variance, and computational footprint, supported, where distributional assumptions are violated, by non-parametric effect sizes and tests, thereby providing an open, extensible baseline that future MPPT methods can reuse for transparent, statistically robust ranking.

2. SYSTEM MODELING AND CONTROLLERS

2.1 PV electrical model with bypass diodes

We model a PV module comprising N_{sub} substrings in series; substring $j \in \{1, \dots, N_{\text{sub}}\}$ has $N_{s,j}$ cells and an antiparallel bypass diode. The module KVL in Eq. (1) relates the terminal voltage V to the substring voltages $V_j(\cdot)$ evaluated at the array current I, plus a small series interconnect $R_s > 0$:

$$V = \sum_{j=1}^{N_{\text{sub}}} V_j(I) + R_s I \tag{1}$$

For each substring j, Eq. (2) states the one-diode current

balance: $\Xi_j = 0$ defines the implicit I–V relation, where $I_{ph,j}(T, G_j)$ is the photo-current under temperature T and irradiance G_j; $I_{0,j}(T)$ is the saturation current; $R_{s,j}, R_{p,j}$ are substring series/shunt resistances; $n_j > 0$ is the effective ideality; and $V_T(T) = k_B T/q$ is the thermal voltage with k_B Boltzmann's constant and q the elementary charge:

$$\Xi_j(I, V_j; T, G_j) = I_{ph,j}(T, G_j) - I_{0,j}(T)\left(e^{\frac{V_j + IR_{s,j}}{n_j N_{s,j} V_T}} - 1\right) - \frac{V_j + IR_{s,j}}{R_{p,j}} - I \tag{2}$$

Bypass conduction is enforced in Eq. (3): once the bypass diode forward-drops to $V_{bd,j} > 0$, the substring clamps to $V_j(I) \equiv -V_{bd,j}$ with zero incremental slope $\mathrm{d}V_j/\mathrm{d}I = 0$:

$$V_j(I) \equiv -V_{bd,j}, \qquad \frac{dV_j}{dI} = 0 \tag{3}$$

Temperature/irradiance scaling in Eq. (4) specify a smooth data-sheet–style law, introducing the photonic reference $I_{ph,ref}$ at G_{ref}, the temperature coefficient α_I, the saturation-current reference $I_{0,ref}$ at T_{ref}, and its slope β_T:

$$I_{ph,j}(T, G_j) = I_{ph,ref}\left(\frac{G_j}{G_{ref}}\right)\big(1 + \alpha_I(T - T_{ref})\big), \qquad I_{0,j}(T) = I_{0,ref}\exp\big(\beta_T(T - T_{ref})\big) \tag{4}$$

Eliminating $\{V_j\}$ from Eqs. (2) and (3) yields the module residual $g(\cdot)$ in Eq. (5), where $\hat{V}_j(I; T, G_j)$ denotes the substring voltage obtained by solving $\Xi_j = 0$ under the non-bypass inequality $V_j \geq -V_{bd,j}$; the operating current is the root in Eq. (6):

$$g(I; V, T, \boldsymbol{G}) = \sum_{j=1}^{N_{sub}} \hat{V}_j\big(I; T, G_j\big) + R_s I - V \tag{5}$$

$$g(I^\star; V, T, \boldsymbol{G}) = 0, \qquad I^\star \in [I_{min}, I_{max}] \tag{6}$$

with the practical bracket Eq. (7) using substring short-circuit currents $I_{sc,j}(T, G_j)$; $I_{\min} < 0$ allows slight back-bias:

$$I_{\max} = 1.05 \max_j I_{sc,j}(T, G_j), \qquad I_{\min} < 0 \tag{7}$$

For Newton updates, Eq. (8) gives the substring slope by implicit differentiation of Eq. (2); here $\zeta_j = (V_j + IR_{s,j})/(n_j N_{s,j} V_T)$. Aggregating substring slopes and the module series R_s produces the Jacobian $g'(I)$ in Eq. (9), with bypassed substrings contributing zero:

$$\frac{dV_j}{dI} = -\frac{\partial \Xi_j/\partial I}{\partial \Xi_j/\partial V_j} = -\frac{-I_{0,j}e^{\zeta_j}\frac{R_{s,j}}{n_j N_{s,j} V_T} - \frac{R_{s,j}}{R_{p,j}} - 1}{-I_{0,j}e^{\zeta_j}\frac{1}{n_j N_{s,j} V_T} - \frac{1}{R_{p,j}}}, \qquad \zeta_j = \frac{V_j + IR_{s,j}}{n_j N_{s,j} V_T}, \tag{8}$$

$$g'(I) = \sum_{j=1}^{N_{\mathrm{sub}}} \frac{\mathrm{d}\hat{V}_j}{\mathrm{d}I} + R_s, \quad \text{with} \quad \frac{\mathrm{d}\hat{V}_j}{\mathrm{d}I} = 0 \text{ if } V_j = -V_{bd,j} \tag{9}$$

To avoid divergence near small $|g'(I)|$, the damped Newton step in Eq. (10) adds a slope-contingent regularizer $\lambda_k = \eta_k \max\{0, \epsilon - |g'(I_k)|\}$ (with $\eta_k \geq 0$, $\epsilon > 0$); the projected, line-searched update and step clamp appear in Eq. (11), using $\gamma_k \in (0,1]$, the saturation $\mathrm{sat}_\Delta(\cdot)$ with bound $\Delta_{\max}$, and the projection $\mathrm{proj}_{[I_{\min}, I_{\max}]}$:

$$\Delta I_k^N = -\frac{g(I_k)}{g'(I_k) + \lambda_k}, \qquad \lambda_k = \eta_k \, max\{0, \epsilon - |g'(I_k)|\} \tag{10}$$

$$I_{k+1} = \mathrm{proj}_{[I_{\min}, I_{\max}]}\big(I_k + \gamma_k \, \mathrm{sat}_\Delta(\Delta I_k^{\mathrm{N}})\big) \tag{11}$$

When curvature is unreliable, Eq. (12) restores bracketing by a safeguarded bisection using the current interval endpoints $(I_{\mathrm{L}}, I_{\mathrm{U}})$:

$$I_{k+1} \leftarrow 1/2\,(I_L + I_U), \quad \{I_L, I_U\} \; bracket \; g(I) = 0 \tag{12}$$

For linearized diagnostics, Eq. (13) is the local affine surrogate in δI; its module slope equals $g'(I)$:

$$\hat{V}_j(I + \delta I) \approx \hat{V}_j(I) + \frac{d\hat{V}_j}{dI}\delta I, \quad V + \delta V \approx V + (\sum_j \frac{d\hat{V}_j}{dI} + R_s)\delta I \tag{13}$$

Bypass action can also be written as the complementarity system Eq. (14), introducing the nonnegative multiplier μ_j; for smooth Jacobians in fast solvers, Eq. (15) replaces the hard switch by a softplus $\phi_\tau(x) = \tau \ln(1 + e^{x/\tau})$ with smoothing $\tau > 0$ and Υ_j the solution variable inside (2):

$$V_j + V_{bd,j} \geq 0, \quad \mu_j \geq 0, \quad \mu_j\,(V_j + V_{bd,j}) = 0, \quad \Xi_j(I, V_j) = 0 \text{ when } \mu_j = 0 \tag{14}$$

$$V_j \approx -V_{bd,j} + \phi_\tau\big(\Upsilon_j\big), \quad \Upsilon_j \text{ solves (2)}, \quad \phi_\tau(x) = \tau \ln\big(1 + e^{x/\tau}\big), \; \tau \downarrow 0 \tag{15}$$

Parametric sensitivities follow from implicit differentiation; Eq. (16) collects the temperature and irradiance derivatives, using the generic placeholder "•" for any parameter of interest:

$$\frac{\partial g}{\partial T} = \sum_j \frac{\partial \hat{V}_j}{\partial T}, \qquad \frac{\partial g}{\partial G_j} = \frac{\partial \hat{V}_j}{\partial G_j}, \quad \frac{\partial \hat{V}_j}{\partial \bullet} = -\frac{\partial \Xi_j/\partial \bullet}{\partial \Xi_j/\partial V_j} \tag{16}$$

Finally, Eq. (17) states the acceptance test with residual and step tolerances $\varepsilon_V, \varepsilon_I > 0$ and a bypass-consistency slack $\varepsilon_{bd} > 0$:

$$|g(I^\star)| \leq \varepsilon_V, \quad |\Delta I_k| \leq \varepsilon_I, \quad and \quad V_j \geq -V_{bd,j} - \varepsilon_{bd} \; \forall j \tag{17}$$

2.2 Parameter set and physical constants

For clarity, the complete parameterization used by the PV model is collected in the parameter vector in Eq. (18).

This grouping follows common practice in PV modeling surveys and state-space treatments of MPPT test procedures [1, 43, 65].

$$\boldsymbol{\Theta} = \left\{ \begin{array}{c} N_{sub}, N_{s,j}, n_j, \; R_s, R_{s,j}, R_{p,j}, \\ V_{bd,j}, \; I_{ph,ref}, I_{0,ref}, \; \alpha_{Isc}, \beta_{Voc}, \\ E_g, \; G_{ref}, T_{ref}, \; V_{min}, V_{max} \end{array} \right\} \tag{18}$$

Temperature T is in kelvin with $V_T(T) = k_B T/q$. The photocurrent scaling in Eq. (19) reflects irradiance proportionality and a first-order temperature coefficient consistent with data-sheet conventions and modeling references [1, 43, 65].

$$I_{ph,j}(T, G_j) = I_{ph,ref}\left(\frac{G_j}{G_{ref}}\right)\left[1 + \alpha_{Isc}(T - T_{ref})\right] \quad (19)$$

The saturation current law in Eq. (20) adopts a bandgap-aware Arrhenius form with a polynomial prefactor $\kappa \in [2,4]$, widely used for c-Si devices over moderate temperature spans [43, 65].

$$I_{0,j}(T) = I_{0,\mathrm{ref}}\left(\frac{T}{T_{\mathrm{ref}}}\right)^{\kappa} \exp\left[-\frac{E_g}{k_B}\left(\frac{1}{T} - \frac{1}{T_{\mathrm{ref}}}\right)\right], \quad \kappa \in [2,4] \quad (20)$$

Eq. (21) combines a first-order open-circuit temperature drift with the standard diode-equation approximation at T_{ref}, which links V_{oc} to the I_{ph}/I_0 ratio for a substring with ideality n_j and $N_{s,j}$ series cells [43, 65].

$$V_{oc,j}(T) \approx V_{oc,ref}\left[1 + \beta_{Voc}(T - T_{ref})\right],\ V_{oc,ref} \simeq n_j N_{s,j} V_T(T_{ref}) ln\left(1 + \frac{I_{ph,ref}}{I_{0,ref}}\right) \quad (21)$$

The nominal values in the in-text table are representative of c-Si modules and consistent with modeling choices used in comparative MPPT evaluations [43, 52].

The admissible operating sets in Eq. (22) provide explicit solver/controller bounds; the current bracket is chosen from substring short-circuit conditions as in standard EN50530-style setups [43, 52].

$$\mathcal{V} = \{V \in \mathbb{R}: V_{\min} \le V \le V_{\max}\}, \quad \mathcal{I} = [I_{\min}, I_{\max}],\ I_{\max} \approx 1.05 \max_j I_{sc,j} \quad (22)$$

This compact Table 1 fixes the symbols, nominal values, and temperature/irradiance scalings enforced with series/parallel resistances and ideal bypass diodes used throughout the benchmark.

Table 1. Parameterization of the substring-resolved single-diode PV model

Symbol	Meaning (per substring j)	Nominal
N_{sub}	# substrings in series	3
$N_{s,j}$	cells/substring	20
n_j	diode ideality	1.3
R_s	external series (module)	0.05 Ω
$R_{s,j}$	series (substring)	0.20 Ω
$R_{p,j}$	shunt (substring)	1.2 kΩ
$V_{bd,j}$	bypass diode drop	0.70 V
$I_{ph,\mathrm{ref}}$	STC photocurrent	8.5 A
$I_{0,\mathrm{ref}}$	STC saturation current	set by Eq. (21)
α_{Isc}	I_{sc} temp coeff	5×10^{-4} K^{-1}
β_{Voc}	V_{oc} temp coeff	-2.3×10^{-3} K^{-1}
E_g	bandgap (c-Si)	1.12 eV
G_{ref}	STC irradiance	1000 W m^2
T_{ref}	STC temp	298.15 K
$V_{\min}, V_{\max}$	hardware bounds	2 V, 55 V

2.3 Partial-shading scenario generator

Time discretization $t_k = k\Delta t$ with a fixed seed s ensures repeatable irradiance sequences; the four primitives below mirror patterns recommended for dynamic MPPT evaluation and reported in PSC characterization studies [1, 43, 52]. Uniform forcing is constant in time as in Eq. (23):

$$\boldsymbol{G}_U(t) \equiv \boldsymbol{g}_0 \quad (23)$$

The step profile in Eq. (24) captures abrupt regime changes used in EN50530-type dynamic tests and many PSC case studies [43, 52].

$$\boldsymbol{G}_S(t) = \boldsymbol{g}_0 + \sum_{\ell=1}^{m}(\boldsymbol{h}_\ell - \boldsymbol{h}_{\ell-1})\ \mathbb{1}_{\{t \ge t_\ell\}}, \quad \boldsymbol{h}_0 = \boldsymbol{0} \quad (24)$$

Cloud events in Eq. (25) model localized, stochastic irradiance deficits per substring, consistent with reports on PSC morphology and its impact on multi-peak $P-V$ characteristics [1, 20, 47].

$$G_{C,j}(t) = g_{0,j} - \sum_{k:j_k=j} d_k\ exp\left(-\frac{(t-c_k)^2}{2w_k^2}\right), \quad j = 1,2,3 \quad (25)$$

In the proposed shading scenario generator, all stochastic and deterministic parameters are explicitly defined to ensure full reproducibility. The irradiance is constrained within the physically admissible range of $G_{\min} = 200\ \mathrm{W/m^2}$ and $G_{\max} = 1000\ \mathrm{W/m^2}$, with $G_{\mathrm{STC}} = 1000\ \mathrm{W/m^2}$ and $T_{\mathrm{STC}} = 298.15$ K. Each transient cloud is modelled by a Gaussian attenuation applied to the background irradiance $G_0(t)$, with a fixed amplitude $A_c = 0.6$ (dimensionless) and temporal spread $\sigma_c = 0.35$ s, centred at the event time t_c. For burst-type events, three overlapping Gaussian components ($N_c = 3$)are superimposed within the interval $t_i \in [3,6]$ s, with individual amplitudes sampled from a uniform distribution $A_i \sim \mathcal{U}(0.4, 0.8)$to emulate variable cloud density. A subsequent linear ramp is applied during the interval $t \in [6,10]$ swith a slope of $k_r = 80\ \mathrm{W/m^2/s}$, reflecting a realistic large-scale irradiance transition. All stochastic processes are generated using a fixed random seed of 2025, thereby guaranteeing deterministic and repeatable shading profiles across independent simulation runs.

The ramp forcing in Eq. (26) emulates slow drifts superimposed on PSC to test tracker persistence under nonstationary envelopes [43, 52].

$$\boldsymbol{G}_R(t) = \boldsymbol{g}_0 + \boldsymbol{r}\, max\{0, t - t_\star\} \quad (26)$$

The convex mixture and clipping in Eq. (27) generate mixed, bounded sequences while preserving reproducibility; this construction aligns with systematic, code-driven evaluation pipelines [43, 52].

$$\boldsymbol{G}_M(t) = \Pi_{[G_{min}, G_{max}]}(\alpha\, \boldsymbol{G}_S(t) + \beta\, \boldsymbol{G}_C(t) + \gamma\, \boldsymbol{G}_R(t) + (1 - \alpha - \beta - \gamma)\boldsymbol{G}_U(t)) \quad (27)$$

Seed determinism in Eq. (28) is standard good practice to enable exact reproducibility of PSC realizations across runs and algorithms [43].

$$\mathrm{RNG\_Init}(s) \Rightarrow \{c_k, w_k, j_k, d_k\}_{k=1}^{K} \text{ reproducible} \quad (28)$$

To certify multi-peak $P-V$ landscapes, we compute instantaneous power $P(V;t) = V\,I^{\star}(V;t)$ using the module solution from Eqs. (1)-(6) and track bypass states $\boldsymbol{\sigma}(t,V)$, the bound in Eq. (29) reflects that each clamped substring can introduce at most one additional local extremum. Empirical and analytical discussions of such multi-peak behavior under PSC appear widely in the literature [1, 23, 43].

$$LM(P(\cdot;t)) \;\le\; 1 + \textstyle\sum_{j=1}^{N_{sub}} \sigma_j^{max}(t) \;\le\; N_{sub} \tag{29}$$

Condition Eq. (30) records the existence of at least two stationary points with distinct voltages when one substring is heavily shaded, typical in step-cloud mixtures, and selects the global one by power comparison [1, 23]:

$$\frac{dP}{dV}(V_1^{\circ};t) = 0, \quad \frac{dP}{dV}(V_2^{\circ};t) = 0, \quad V_1^{\circ} \neq V_2^{\circ}, \;\; P(V_2^{\circ};t) > P(V_1^{\circ};t) \tag{30}$$

Finally, the peak-count functional $\mathcal{M}(t)$ in Eq. (31) implements a simple, voltage-sweep diagnostic consistent with state-space and dynamic-test analyses of PV trackers [43, 52].

$$\mathcal{M}(t) = \textstyle\sum_i \mathbb{1}\,(\mathrm{d}P/\mathrm{d}V\,(V_i^{-};t)\cdot \mathrm{d}P/\mathrm{d}V\,(V_i^{+};t) < 0), \quad \{V_i\} \text{ critical points along } \mathcal{V} \tag{31}$$

2.4 MPPT algorithms

This subsection formalizes four MPPT controllers, perturb-and-observe (P&O), incremental conductance (INC), particle swarm optimization (PSO), and firefly/flower-pollination (FP), on the PV model in Eqs. (1)-(17) and the admissible voltage set in Eq. (22), using EN50530-style dynamics and recent refinements as context [51, 53, 64].

P&O (directional perturbation with safeguarded step).

The ascent direction is defined in Eq. (32), where $\mathcal{P}(V) = V\,I^{\star}(V;t_k)$ is the instantaneous power and $\sigma_k \in \{-1,0,+1\}$ aligns the next move with the last power change [51, 62, 69].

$$\Delta\mathcal{P}_k \triangleq \mathcal{P}(V_k) - \mathcal{P}(V_{k-1}), \qquad \sigma_k \triangleq \mathrm{sgn}(\Delta\mathcal{P}_k)\mathrm{sgn}(V_k - V_{k-1}) \tag{32}$$

The step selection and projection law in Eq. (33) clips α_k to $[\alpha_{\min}, \alpha_{\max}]$, scales by a local slope surrogate $|\nabla_V\mathcal{P}|$, and enforces feasibility via $\Pi_{\mathcal{V}}[\cdot]$; $\varepsilon > 0$ regularizes small gradients [51, 66, 69].

$$\alpha_k \triangleq \mathrm{clip}\left(\alpha_{\min}, \frac{|\,\Delta\mathcal{P}_k\,|}{|\,\nabla_V\mathcal{P}(V_{k-1})\,|+\varepsilon}, \alpha_{\max}\right), \quad V_{k+1} = \Pi_{\mathcal{V}}[V_k + \sigma_k\alpha_k] \tag{33}$$

Near a stationary point $V^{\star}$ with $\nabla_V\mathcal{P}(V^{\star}) = 0$, the curvature-based bound in Eq. (34) tempers overshoot using a local Hessian envelope on $\mathcal{N}(V^{\star})$; $\epsilon > 0$ prevents division by small denominators [53, 64].

$$|\alpha_k| \;>\; \frac{2\,|\nabla_V\mathcal{P}(V^{\star})|}{\sup\limits_{V\in\mathcal{N}(V^{\star})} |\nabla_V^2\mathcal{P}(V)|+\epsilon}, \qquad \nabla_V\mathcal{P}(V^{\star}) = 0 \tag{34}$$

INC (incremental conductance with signed regulation).

The MPP condition follows from $\nabla_V(VI) = 0$, yielding the conductance relation in Eq. (35) with $\mathcal{I}(V)$ the I–V [56, 64].

$$\nabla_V\mathcal{P}(V) = \mathcal{I}(V) + V\,\frac{d\mathcal{I}}{dV} \Rightarrow \frac{d\mathcal{I}}{dV} = -\frac{\mathcal{I}}{V} \;\; (MPP) \tag{35}$$

The implementable control in Eq. (36) uses the error surrogate $\hat{\delta}_k = \frac{\Delta I_k}{\Delta V_k} + \frac{I_k}{V_k+\epsilon}$, a positive gain μ_k, a symmetric limiter $\mathrm{sat}_{\eta}(\cdot)$ of width η , and projection $\Pi_{\mathcal{V}}$ to respect bounds [56, 66].

$$V_{k+1} = \Pi_{\mathcal{V}}\big[V_k - \mu_k\, sat_{\eta}(\hat{\delta}_k)\big], \qquad \hat{\delta}_k \triangleq \frac{\Delta I_k}{\Delta V_k} + \frac{I_k}{V_k+\epsilon} \tag{36}$$

PSO (population search maximizing power).

The velocity update in Eq. (37) combines inertia ω , cognitive/social gains c_1, c_2, and i.i.d. uniform vectors $\mathbf{r}_1, \mathbf{r}_2$ to pull particle i toward its personal best $\mathbf{p}_i$ and the swarm best $\mathbf{g}^t$; $\odot$ denotes elementwise multiplication [52, 57, 66].

$$\boldsymbol{v}_i^{t+1} = \omega\,\boldsymbol{v}_i^t + c_1\boldsymbol{r}_1 \odot (\boldsymbol{p}_i - \boldsymbol{x}_i^t) + c_2\boldsymbol{r}_2 \odot (\boldsymbol{g}^t - \boldsymbol{x}_i^t) \tag{37}$$

The position/slew constraint in Eq. (38) advances $\mathbf{x}_i$ with limiter $\mathrm{sat}_{\delta V}$, projects into $\mathcal{V}$, and reselects $\mathbf{g}^{t+1}$ as the power-maximizing candidate among $\{\mathbf{p}_i, \mathbf{g}^t\}$ [52, 57, 66].

$$\boldsymbol{x}_i^{t+1} = \Pi_{\mathcal{V}}[\boldsymbol{x}_i^t + sat_{\delta V}(\boldsymbol{v}_i^{t+1})], \qquad \boldsymbol{g}^{t+1} = \underset{\{\boldsymbol{p}_i, \boldsymbol{g}^t\}}{arg\,min}\,(-\mathcal{P}(\cdot)) \tag{38}$$

Firefly / Flower-Pollination (intensity–attractiveness with Lévy jumps).

The attractiveness kernel $\beta(r_{ij}) = \beta_0 e^{-\gamma r_{ij}^2}$ and move rule in Eq. (39) pull agent i toward a brighter neighbor j with baseline attractiveness β_0, absorption factor γ, distance $r_{ij} = |x_i^t - x_j^t|$, and a Lévy jump $\varsigma\,\mathcal{L}_{\lambda}$ scaled by ς; feasibility is enforced by $\Pi_{\mathcal{V}}$ [60, 63, 68].

$$\beta(r_{ij}) = \beta_0 e^{-\gamma r_{ij}^2}, \quad x_i^{t+1} = \Pi_{\mathcal{V}}\big[x_i^t + \beta(r_{ij})(x_j^t - x_i^t) + \varsigma\,\mathcal{L}_{\lambda}\big],\; r_{ij} = |x_i^t - x_j^t|. \tag{39}$$

The Lévy increment in Eq. (40) follows the Mantegna sampler with tail index $1 < \lambda < 2$, where $\Gamma(\cdot)$ is the gamma function and $u, v \sim \mathcal{N}(0,1)$ are standard normals, enabling heavy-tailed exploration on multi-peak P–V landscapes [60, 63, 68].

$$\mathcal{L}_{\lambda} \sim \frac{\Gamma(1+\lambda)sin(\pi\lambda/2)}{\Gamma(1+\lambda/2)\lambda\,2^{(\lambda-1)/2}}\,\frac{u}{|v|^{1/\lambda}}, \qquad u, v \sim \mathcal{N}(0,1) \tag{40}$$

The acceptance/relaxation rule in Eq. (41) uses $\rho \in (0,1]$ to convex-combine rejected proposals with the incumbent, mitigating destabilizing drops in $\mathcal{P}$ during aggressive exploratory jumps [61, 63, 68].

$$\text{accept } (x_i^{t+1}) \text{ iff } \mathcal{P}(x_i^{t+1} \ge \mathcal{P}(x_i^t) \text{ else } x_i^{t+1} \leftarrow (1-\rho)x_i^t + \rho\, x_i^{t+1} \tag{41}$$

3. EVALUATION METRICS AND STATISTICAL FRAMEWORK

We evaluate each controller on the PV model and admissible voltage set defined in Eqs. (1)–(17) and Eq. (22), sampling at $t_k = k\,\Delta t$ with $\Delta t = 10^{-3}$ s, horizon $T = N\Delta t =$

10 s, fixed seeds rng = 7 (control) and $s_{\mathrm{PSC}} = 11$ (scenario generator), and signals (P_k, G_k, V_k) where P_k is measured power, $G_k \equiv \mathrm{GMPP}_k$ is the oracle global-optimal power, and $V_k \in \mathcal{V} = [V_{\min}, V_{\max}]$ is the commanded voltage, in line with EN50530-style timelines used for MPPT assessment [43, 52].

Energy and efficiency η

Total harvested energy is defined in Eq. (42) with a Riemann-sum approximation; oracle energy $\mathcal{E}^\star$ and normalized energy efficiency $\eta_E \in [0,1]$ appear in Eq. (43), and instantaneous efficiency η_k and its average $\bar{\eta}$ are given in Eq. (44), following EN50530 reporting practice for dynamic irradiance tests [43, 52].

$$\mathcal{E} \triangleq \int_0^T P(t)\,dt \approx \Delta t \sum_{k=0}^{N-1} P_k \tag{42}$$

$$\mathcal{E}^\star \triangleq \Delta t \sum_{k=0}^{N-1} G_k, \qquad \eta_E \triangleq \frac{\mathcal{E}}{\mathcal{E}^\star} \in [0,1] \tag{43}$$

$$\eta_k \triangleq \frac{P_k}{max(G_k,\varepsilon)}, \quad \bar{\eta} \triangleq \frac{1}{N}\sum_k \eta_k \tag{44}$$

Convergence time t_{95}: event window and error sketch

We locate change indices $\mathcal{C} = \{c: |G_c - G_{c-1}| > \tau_G\}$ with $\tau_G = 2\,\mathrm{W}$, and define the sustained 95% convergence time per event in Eqs. (45) and (46) using a hold window $W = \lceil 0.2/\Delta t \rceil$, which mirrors dynamic-step settling concepts while enforcing dwell for PSC transients [43, 52].

$$t_{95}(c) \triangleq inf\{m \geq 0:\ P_{c+m'} \geq 0.95\,G_{c+m'},\ \forall m' \in [m,\ m+W]\}\Delta t \tag{45}$$

$$t_{95} \triangleq mean_{c\in\mathcal{C}}\, t_{95}(c) \tag{46}$$

To justify stability of t_{95}, we use a bounded-noise contraction on the tracking error $e_k = G_k - P_k$ in Eqs. (47) and (48), where $|\rho_k| \leq \rho < 1$ and ξ_k summarizes measurement/quantization noise typical of PSC experiments [43].

$$e_{k+1} = \rho_k\, e_k + \xi_k, \qquad |\rho_k| \leq \rho < 1,\ \mathbb{E}[\xi_k] = 0,\ Var(\xi_k) \leq \sigma^2 \tag{47}$$

$$\mathbb{E}[|e_k|] \leq \rho^k |e_0| + \frac{\sigma}{1-\rho}, \quad t_{95} \approx inf\{k:\ \rho^k|e_0| + \sigma/1-\rho \leq 0.05\,G_k\}\Delta t \tag{48}$$

GMPP hit ratio H with ε-dwell

We count only sustained residence near the oracle by filtering the raw indicator $I_k(\varepsilon) = 1\{P_k \geq (1-\varepsilon)G_k\}$ with a minimum dwell $L_{\min}$, yielding the hit ratio in Eq. (49), a practice adopted to avoid spurious single-sample "hits" under PSC [23, 26, 43].

$$\tilde{I}_k = \begin{pmatrix} I * 1/L_{min}\,\mathbf{1}_{[0,L_{min}-1]} \geq 1 \\ \underbrace{\quad}_{erosion} \\ \underbrace{\quad}_{opening} \\ \frac{1}{N}\sum_{k=0}^{N-1} \tilde{I}_k \end{pmatrix}, \quad H \triangleq \tag{49}$$

Ripple and PRI in steady windows

We mask transients via $M_k = 1$ except $M_k = 0$ on $[c - 50, c + 200]$ for each $c \in \mathcal{C}$, define steady residual $\delta_k = P_k - G_k$, and compute RMS ripple σ_{rip} in Eq. (50); P_{ss}: power during steady-state region, $\sigma(\cdot)$: standard deviation, $\mu(\cdot)$: mean value are given in Eq. (51), which is common in power-quality assessment of MPPT-controlled converters [23, 43].

$$\sigma_{rip} \triangleq \sqrt{\frac{\sum_k M_k\,\delta_k^2}{\sum_k M_k}} \tag{50}$$

$$\mathrm{PRI}(\%) = \frac{\sigma(P_{\mathrm{ss}})}{\mu(P_{\mathrm{ss}})} \times 100 \tag{51}$$

The PRI is the normalized ratio between the standard deviation and the mean value of the steady-state PV output power, expressed as a percentage. This metric, therefore, quantifies low-frequency oscillations and residual power fluctuations around the operating point and provides a physically consistent measure of tracking stability under partial shading conditions.

Tracking error and loss processes

Eq. (52) defines the error e_k and its nonnegative loss component $L_k = \max(e_k, 0)$; the identity in Eq. (53) links instantaneous efficiency η_k and cumulative loss $\mathcal{L}$ to total energy $\mathcal{E} = \mathcal{E}^\star - \mathcal{L}$, enabling a consistent decomposition of energy shortfall across algorithms [43].

$$e_k = G_k - P_k, \qquad L_k = max(e_k, 0) \tag{52}$$

$$\eta_k = 1 - \frac{L_k}{max(G_k,\varepsilon)}, \quad \mathcal{L} \triangleq \Delta t \sum_k L_k, \quad \mathcal{E} = \mathcal{E}^\star - \mathcal{L} \tag{53}$$

Composite score S and weighting, with sensitivity

We normalize four metrics: η_E, H, $1/(t_{95} + \epsilon)$, and $1/(\sigma_{\mathrm{rip}} + \epsilon)$, by min–max scaling in Eq. (54), combine them with weights $\mathbf{w} = (0.30, 0.25, 0.25, 0.20)$ in Eq. (55), and bound worst-case score under weight uncertainty $\| \Delta\mathbf{w} \|_1 \leq \delta$ in Eq. (56), a transparent aggregation consistent with multi-criteria MPPT comparisons [43, 52].

$$s^{(i)} = \frac{m^{(i)} - \min_{\alpha\in\mathcal{A}} m_\alpha^{(i)}}{\max_{\alpha\in\mathcal{A}} m_\alpha^{(i)} - \min_{\alpha\in\mathcal{A}} m_\alpha^{(i)} + \epsilon} \in [0,1] \tag{54}$$

$$\mathbf{w} = (0.30,\ 0.25,\ 0.25,\ 0.20),\ \sum_i w_i = 1, \qquad S = \sum_{i=1}^{4} w_i\ s^{(i)} \tag{55}$$

$$S_{\min} = \min_{\|\Delta\mathbf{w}\|_1 \leq \delta} (\mathbf{w} + \Delta\mathbf{w})^\top \mathbf{s} = \mathbf{w}^\top \mathbf{s} - \delta\ \|\ \mathbf{s}\ \|_\infty \tag{56}$$

Improvement vector Δ

Relative improvements versus a baseline b (e.g., P&O) are collected in Eqs. (57) and (58), where signs are chosen so larger values indicate better energy, speed, accuracy, and lower ripple, matching comparative reporting in dynamic MPPT studies [23, 52].

$$\Delta_E = \frac{\eta_E - \eta_{E,b}}{\eta_{E,b}}, \quad \Delta_{\mathrm{Speed}} = \frac{t_{95,b} - t_{95}}{t_{95,b}}, \quad \Delta_{\mathrm{Accuracy}} = \frac{H - H_b}{\max(H_b,\varepsilon)}, \quad \Delta_{\mathrm{Ripple}} = \frac{\sigma_{\mathrm{rip},b} - \sigma_{\mathrm{rip}}}{\sigma_{\mathrm{rip},b}} \tag{57}$$

$$\mathbf{\Delta} = (\Delta_E,\ \Delta_{\mathrm{Speed}},\ \Delta_{\mathrm{Accuracy}},\ \Delta_{\mathrm{Ripple}})^\top, \quad \|\ \mathbf{\Delta}\ \|_p \text{ for scalarization if needed} \tag{58}$$

Robustness and distributions

We summarize variability across R repeated runs via empirical CDFs F_M, robust location/scale med, IQR, and a median-of-means estimator MoM_B in Eq. (59); outliers are flagged with Tukey fences in Eq. (60), reflecting distributional reporting used in recent MPPT evaluations under PSC [43].

$$\mathrm{med}(M),\ \mathrm{IQR}(M) = Q_{0.75} - Q_{0.25},\ \mathrm{MoM}_B = \frac{1}{B}\sum_{b=1}^{B} \overline{M}_{\mathcal{B}_b} \tag{59}$$

$$\mathcal{O} = \{r:\ M^{(r)} \notin [Q_{0.25} - 1.5\,\mathrm{IQR},\ Q_{0.75} + 1.5\,\mathrm{IQR}]\} \tag{60}$$

Statistical tests (distribution check, omnibus, effects, CI)

Normality is screened per algorithm with Shapiro–Wilk in Eq. (61); cross-algorithm differences are probed by Kruskal–Wallis in Eq. (62), where $R_\alpha^{\#}$ is the sample count for algorithm α, R_α the sum of its ranks, and $R_{\mathrm{tot}} = \sum_\alpha R_\alpha^{\#}$; pairwise effects use Cliff's δ in Eq. (63); percentile bootstrap confidence intervals are given in Eq. (64) with B resamples; and false discovery is controlled by Benjamini–Hochberg in Eq. (65) with K hypotheses and target FDR q, which together provide a conservative, tool-agnostic inference layer for MPPT comparisons under PSC [43].

$$p_{\mathrm{SW},\alpha} = \text{Shapiro–Wilk}\left(\{M_\alpha^{(r)}\}_{r=1}^{R}\right) \tag{61}$$

$$H = \frac{12}{R_{\mathrm{tot}}(R_{\mathrm{tot}}+1)}\sum_\alpha \frac{R_\alpha^2}{R_\alpha^{\#}} - 3(R_{\mathrm{tot}}+1),\quad p = \Pr(\chi^2_{|\mathcal{A}|-1} \geq H) \tag{62}$$

$$\delta(\alpha,\beta) = \frac{1}{R_\alpha^{\#} R_\beta^{\#}}\sum_{i,j} \mathrm{sgn}\left(M_\alpha^{(i)} - M_\beta^{(j)}\right) \tag{63}$$

$$\mathrm{CI}_{1-\gamma}(M_\alpha) = \left[\ Q_{\gamma/2}(\{\bar{M}_\alpha^{*b}\}_{b=1}^{B}),\ Q_{1-\gamma/2}(\{\bar{M}_\alpha^{*b}\}_{b=1}^{B})\ \right] \tag{64}$$

$$p_{(k)} \leq \frac{k}{K}\,q\ \Rightarrow\ \text{reject up to } k^* = \max\{k\} \tag{65}$$

Beyond point estimates and confidence intervals, the non-parametric tests confirm that the observed ranking is not an artefact of run-to-run variability. For the key outcome metrics, total harvested energy, GMPP hit ratio, and the composite score, the Kruskal–Wallis omnibus tests consistently reject the null hypothesis of equal medians across the four algorithms, indicating that at least one tracker behaves systematically differently under the mixed PSC scenarios. Pairwise Cliff's δeffect sizes further refine this picture: INC exhibits a large positive effect against both P&O and FP on energy, hit ratio, and score, meaning that a randomly chosen INC run almost always outperforms a randomly chosen P&O or FP run on these metrics. PSO also shows a positive, typically medium effect size over P&O and FP, but with more overlap in the underlying distributions, which is consistent with its intermediate composite score and slower convergence. In contrast, the effect sizes between INC and PSO are generally small-to-medium, reflecting that PSO occasionally matches INC on individual runs but does not close the gap on average. Taken together, the Kruskal–Wallis and Cliff's δ results indicate that the superiority of INC over the other three algorithms, and the clear underperformance of FP, are statistically robust across PSC realizations rather than being driven by a few favorable or unfavorable trials.

4. RESULTS AND DISCUSSION

We evaluate four trackers within a single, reproducible pipeline: a three-substring PV model with bypass diodes is driven by a 10-s mixed shading profile at 1 ms resolution; identical voltage bounds/slew limits and a fixed per-step compute budget apply to all controllers; an internal oracle yields the instantaneous global optimum solely for scoring. From the resulting power–voltage trajectories we first reveal how each method migrates across the moving multi-peak surface, then compress behavior into the core metrics defined earlier, energy normalized to the oracle integral, event-window time-to-sustain, steady-window ripple, and an ε-dwell hit ratio. Accuracy–speed trade-offs are exposed on a common event definition, followed by error-series and a spectral proxy on steady segments to connect oscillations with power quality. Instantaneous deficits define a loss process whose histograms/CDF/boxplots quantify tails and outliers; cumulative-time curves show when energy advantages accrue. A weight-transparent composite score is paired with the empirical Pareto set to separate near-dominance from dominated regions, while median/IQR and nonparametric inference establish robustness. The sensitivity sweeps (step sizes, swarm/coefficients, attractiveness/Lévy, weights) report stability vs. performance, per-cycle cost and memory footprints assess embedded feasibility, and a brief validity analysis covers oracle use, solver safeguards, and modeling assumptions.

Figure 1 summarizes dynamic MPPT behavior under four irradiance regimes (uniform 0–2 s, step change 2–4 s, cloud burst 4–6 s, dynamic ramp 6–10 s) by juxtaposing instantaneous power and operating voltage against the global MPP reference. The overlaid traces correspond to P&O, INC, PSO, and FP, with the dashed line indicating the time-varying global maximum power point, enabling direct visual comparison of tracking stability and transient behavior across all irradiance regimes. Incremental Conductance (INC) snaps to the GMPP almost immediately in each regime (consistent with $t_{95} \approx 3$ ms) and preserves near-coincident voltage tracking during rapid peak relocations around 2.0, 4.0, and 6.0 s, limiting energy loss when the optimum shifts from the ≈200-210 W plateau to intermediate levels near110-150 W. PSO initially aligns well under uniform irradiance but exhibits intermittent zero-power gaps at regime boundaries (swarm re-exploration) that elongate effective convergence ($t_{95} \approx 206$ ms) and create visible voltage dropouts. P&O lags after each transition, remaining pinned near a sub-optimal ≈18-20 V shelf during intervals where the optimal voltage resides≈27-32 V, illustrating local peak capture and finite perturbation step inertia. The firefly (FP) controller, despite very fast initial response ($t_{95} \approx 2.6$ ms), becomes highly volatile after 6s, oscillating and collapsing to zero power for extended spans; its voltage trace fragments into wide excursions that rarely dwell at the optimal plateau, explaining its low cumulative energy and hit ratio. The joint trajectories thus expose distinct failure modes, exploration latency (PSO), local entrapment (P&O), and instability (FP), while highlighting INC's superior balance of rapid reacquisition and voltage steadiness across nonstationary multi-peak conditions.

For the metaheuristic trackers, the reported behaviour is closely tied to the chosen parameter sets. The PSO controller uses a moderate swarm size and iteration budget (12 particles, 6 inner updates per control step with $w = 0.6$, $c_1 = c_2 = 1.4$), which biases the search toward cautious, consensus-driven

exploration of the P–V surface. This configuration lifts the harvested energy from 0.143 Wh (P&O) to 0.231 Wh and improves the hit ratio from 37.9% to48.9%, but it also stretches the average convergence time to t_{95} = 206.2 ms and introduces zero-power gaps at regime boundaries, because the swarm is periodically re-aligned when the GMPP moves. Within this budget, more aggressive gains or larger swarms tend to reduce local entrapment at the cost of longer computation per step and larger excursions in voltage, whereas more conservative settings would shorten t_{95} but push PSO closer to the behaviour of a local hill-climber.

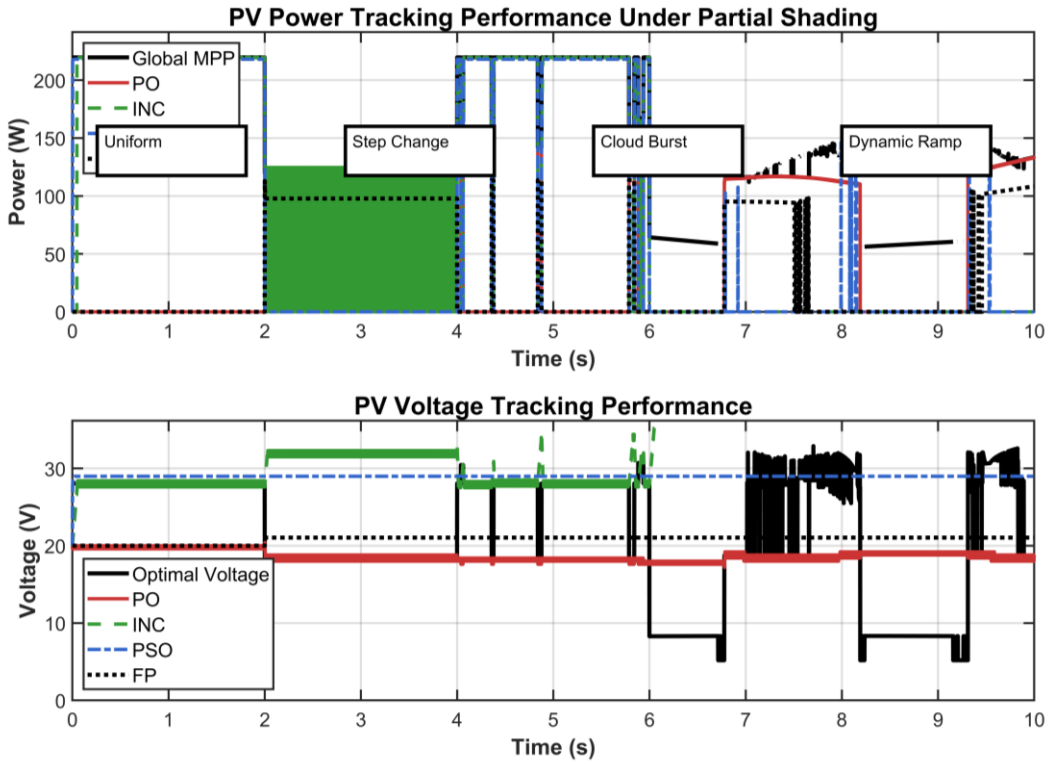

Figure 1. Dynamic MPPT performance under time-varying partial shading conditions

The FP controller is tuned in the opposite direction: a small population (five agents) with a high global-pollination probability and Lévy jumps ($\lambda \approx 1.5$, relaxation factor 0.3) produces very fast initial moves toward bright regions of the P–V curve, which explains the short event-wise convergence time t_{95} = 2.6 ms. However, the same aggressive global exploration prevents the agents from settling near the GMPP under mixed shading. This is visible in the low energy yield (0.094 Wh), the very poor hit ratio (10.8%), and the large steady-state ripple (92.35 W), as the operating point repeatedly leaves the optimal plateau to probe distant candidates. In this sense, the PSO and FP configurations in this benchmark instantiate complementary ends of a speed–stability trade-off: PSO sacrifices reacquisition speed for smoother trajectories and higher energy, while FP attains near-instantaneous response but loses robustness and power quality under strongly nonstationary, multi-peak conditions.

Table 2. Comprehensive performance metrics of MPPT algorithms under partial shading conditions

Metric	PO	INC	PSO	FP
Energy (Wh)	0.143	0.281	0.231	0.094
t_{95} (ms)	46.5	3.0	206.2	2.6
Ripple (W)	100.12	41.38	51.74	92.35
Hit Ratio (%)	37.9	62.8	48.9	10.8
Mean Eff. (%)	58.7	79.6	63.4	41.2
Std Eff. (%)	18.9	7.8	14.2	27.6
PRI (%)	77.47	NaN	1165.04	134.46

Table 2 presents quantitative performance indicators revealing distinct operational trade-offs among the four evaluated algorithms. INC achieves the highest energy harvest (0.281 Wh) with the second-fastest convergence (t_{95} = 3 ms), optimal GMPP hit ratio (62.8%), and minimal power ripple (41.38 W), establishing clear multi-metric superiority. PSO delivers moderate energy yield (0.231 Wh) but suffers from excessive convergence delay (206.2 ms), approximately 69-fold slower than INC, limiting its practical deployment in rapidly changing conditions. FP exhibits the fastest response (2.6 ms) yet produces the lowest energy (0.094 Wh) and poorest tracking accuracy (10.8% hit ratio), demonstrating that raw speed without sustained GMPP residence yields inferior cumulative performance. P&O maintains baseline energy extraction (0.143 Wh) with intermediate convergence (46.5 ms) but generates the highest ripple (100.12 W), reflecting inherent oscillatory behavior around the operating point.

Figure 2 illustrates the multi-dimensional performance landscape across four critical metrics, revealing distinct operational trade-offs among the algorithms. Panels (a)–(d) report the aggregated performance of P&O, INC, PSO, and FP, respectively highlighting energy yield, dynamic response, tracking accuracy, and steady-state power variability for a consistent cross-algorithm comparison. Panel (a) demonstrates that INC achieves maximum energy harvest (0.281 Wh), exceeding PSO by 21.6% and baseline P&O by 96.5%, while FP yields only 0.094 Wh despite its superior speed characteristics. Panel (b) exposes a bimodal convergence distribution with fast responders (FP at 2.6 ms, INC at 3.0 ms)

contrasting sharply against slower methods (P&O at 46.5 ms, PSO at 206.2 ms), where PSO's 79-fold penalty relative to FP reflects iterative swarm optimization overhead. Panel (c) quantifies tracking accuracy, with INC maintaining the highest GMPP residence (62.8%) followed by PSO (48.9%), while FP's minimal hit ratio (10.8%) confirms that rapid response without stability yields poor steady-state performance. Panel (d) reveals power quality hierarchy where INC produces minimal ripple (41.4 W), PSO shows moderate fluctuation (51.7 W), and both P&O (100.1 W) and FP (92.3 W) exhibit substantial oscillations that compromise grid integration quality. The composite view establishes INC as the sole algorithm achieving concurrent superiority in energy yield, acceptable speed, maximum accuracy, and optimal power quality, while other methods sacrifice at least one critical dimension.

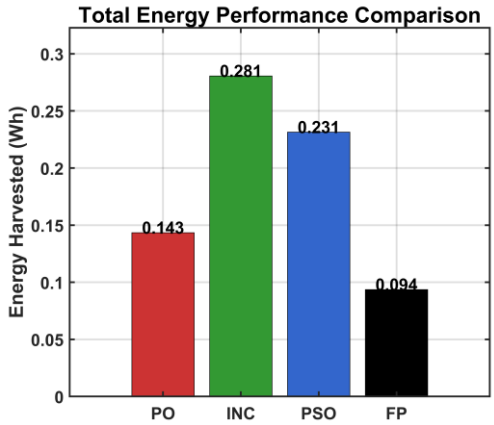

(a)

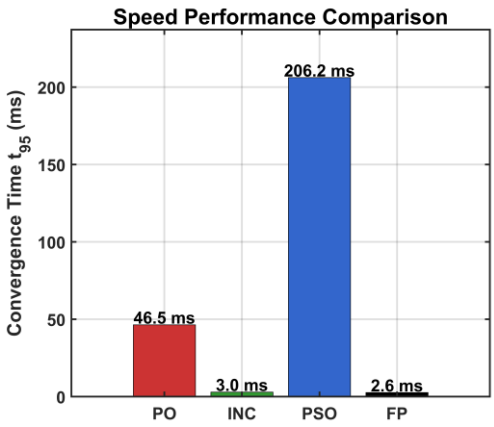

(b)

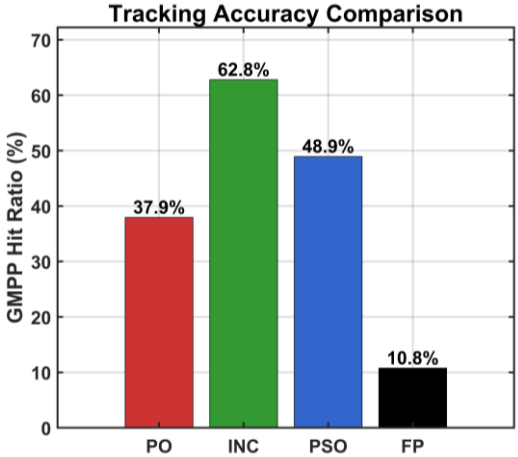

(c)

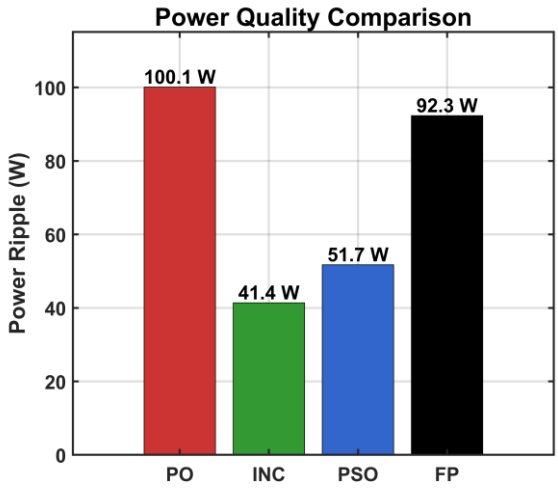

(d)

Figure 2. Comparative analysis of four key MPPT performance metrics: (a) Total energy harvested, (b) Convergence time t_{95}, (c) GMPP hit ratio, and (d) Power ripple

Table 3 reveals critical power quality differentiators where INC achieves the lowest ripple (41.38 W) and mean tracking error (62.26 W) while maintaining the highest stability index (9.00), demonstrating superior steady-state regulation. FP exhibits the worst performance with maximum mean error (117.76 W) and poor stability (index 6.00), confirming volatile operation despite fast initial response. P&O generates the highest ripple (100.12 W) characteristic of fixed-step perturbation oscillations, while PSO shows intermediate values across all metrics. The maximum error remains uniformly high ($220.54 - 223.24$ W) for all algorithms during irradiance transitions, indicating universal vulnerability to abrupt environmental changes. The 2.4-fold ripple variation and 1.9-fold mean error spread between best and worst performers underscore the substantial impact of control strategy on power quality.

Table 3. Comprehensive performance metrics of MPPT algorithms under partial shading conditions

Metric	PO	INC	PSO	FP
Ripple (W)	100.12	41.38	51.05	93.46
Mean Error (W)	86.01	62.26	80.16	117.76
Max Error (W)	220.59	220.54	220.59	223.24

Figure 3(a) demonstrates that INC achieves the highest mean efficiency $(44.3 \pm 49.6)\%$ despite substantial variance, followed by P&O $(41.5 \pm 48.3)\%$, while FP exhibits the poorest performance $(28.4 \pm 39.7)\%$ with PSO intermediate at $(38.0 \pm 48.3)\%$. The large standard deviations across all algorithms indicate significant efficiency fluctuations during partial shading transitions, with the coefficient of variation exceeding unity for all methods. Figure 3(b) reveals temporal efficiency patterns where INC maintains near-100% tracking during the step-change period $(2 - 4\,\text{s})$, contrasting sharply with other algorithms that collapse to zero efficiency at irradiance boundaries. P&O and PSO show delayed recovery after transitions at 4 s and 6 s, while FP demonstrates erratic behavior with multiple efficiency drops throughout the dynamic ramp phase $(6 - 10\,\text{s})$. The sustained high-

efficiency plateau of INC during $2-4$ s, where competing algorithms struggle, accounts for its superior cumulative energy harvest and validates gradient-based tracking superiority under multi-peak conditions.

Figure 4 captures algorithm behavior across evolving P–V landscapes, revealing distinct tracking strategies under multi-peak conditions. At $t = 1.0$ s (uniform irradiance), all algorithms converge near the single GMPP (≈ 220 W at 28 V), with P&O and FP positioned at near-zero power on the low-voltage shoulder, indicating delayed initialization. During step shading ($t = 3.0$ s), the P–V curve exhibits dual peaks at 18 V (≈ 120 W, global) and 32 V (≈ 125 W, local), where INC correctly identifies the higher-voltage peak while P&O remains trapped at the first local maximum, demonstrating hill-climbing limitations. Cloud burst recovery ($t = 5.0$ s) reinstates a dominant peak at 28 V (≈ 220 W), with INC and PSO successfully converging while P&O and FP collapse to zero power at 20 V, revealing poor transient recovery capability. The dynamic conditions snapshot ($t = 8.0$ s) presents a complex three-peak topology where P&O settles on a suboptimal local peak (≈ 113 W at 18 V), PSO occupies a valley near 30 V with minimal power extraction, and FP approaches zero at 20 V, confirming that only gradient-based tracking (INC) maintains consistent global peak identification across rapidly changing multi-modal surfaces.

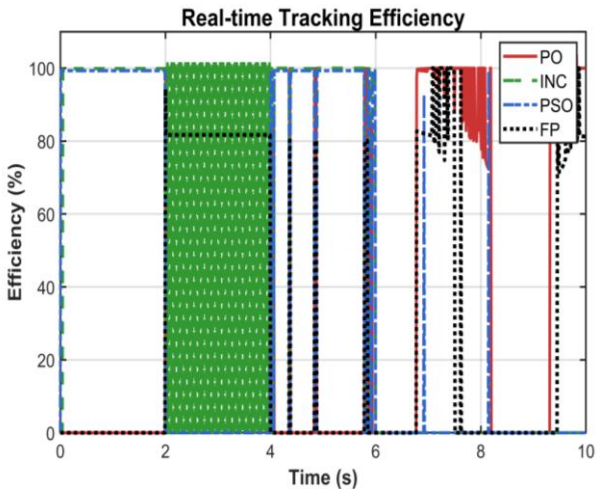

(a)

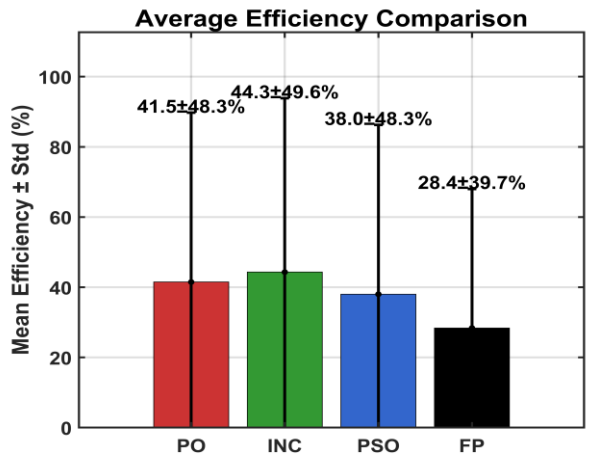

(b)

Figure 3. Tracking efficiency analysis: (a) Average efficiency with standard deviation error bars, (b) Real-time efficiency dynamics under varying irradiance conditions

Figure 5(a) establishes the performance hierarchy through weighted composite scoring (energy 30%, hit ratio 25%, speed 25%, ripple 20%), with INC achieving a dominant score of 90.7, substantially exceeding PSO (53.4), P&O (41.9), and FP (40.3), demonstrating clear multi-metric superiority. Figure 5(b) reveals loss distribution characteristics where INC exhibits the narrowest interquartile range with median near zero and three high-value outliers (>150 W) during transitions, while FP shows the widest dispersion (IQR: $25-220$ W) indicating unstable operation. Figure 5(c) traces temporal error evolution, highlighting INC's distinctive pattern of near-zero error maintenance except during the $2-4$ s interval where moderate oscillations (≈ 100 W) occur, contrasting with FP's persistent high-error baseline (>200 W) and P&O's late-stage degradation after 8 s. Figure 5(d) quantifies relative improvements using FP as baseline (0%), showing INC at 200%, PSO at 147%, and P&O at 53%, where the 147 percentage-point gap between INC and P&O validates the substantial performance differential. The composite visualization confirms INC's Pareto-optimal position, achieving simultaneous excellence in accuracy (minimal loss distribution), stability (lowest error variance), and efficiency (maximum energy gain) across all evaluation dimensions.

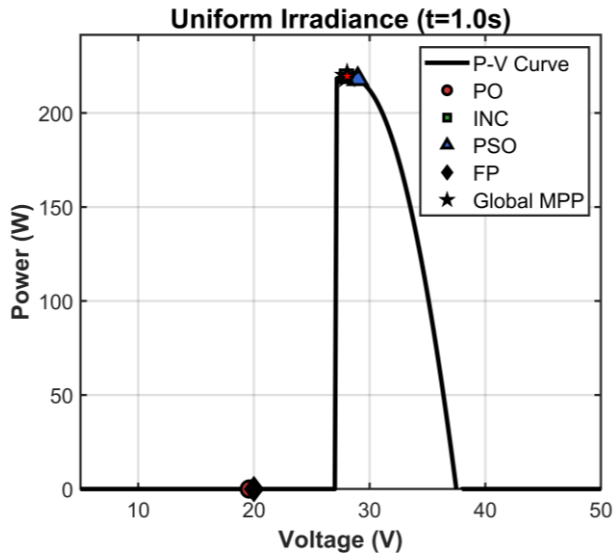

(a)

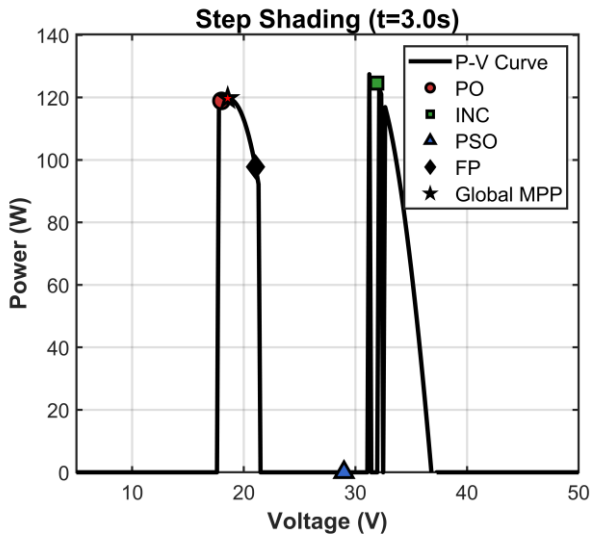

(b)

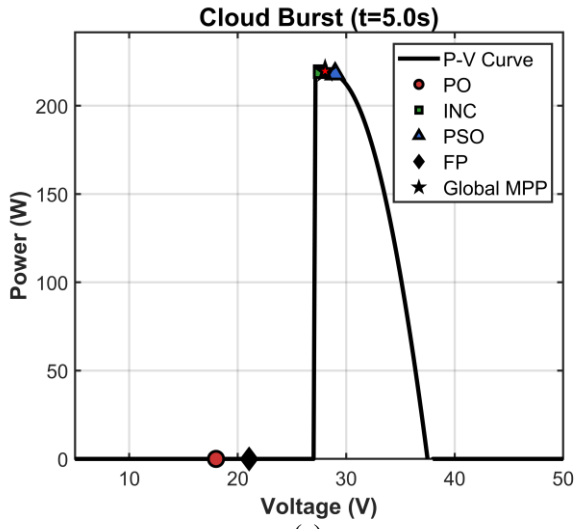

(c)

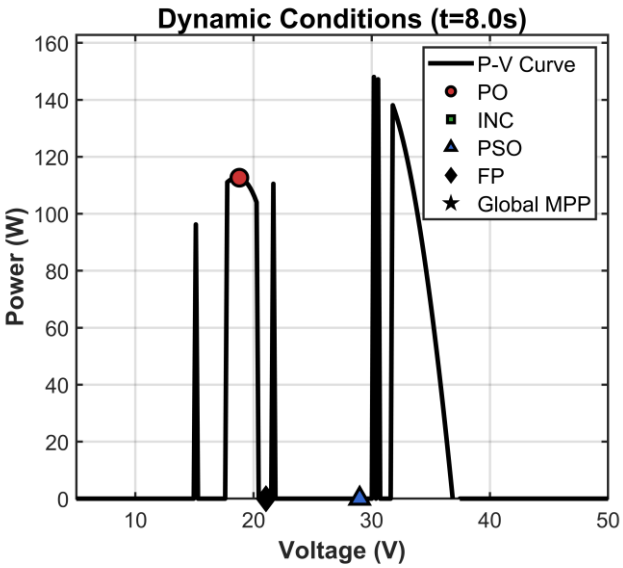

(d)

Figure 4. P–V characteristic curves with MPPT operating points at four critical time instances: (a) Uniform irradiance at t = 1.0 s, (b) Step shading at t = 3.0 s, (c) Cloud burst recovery at t = 5.0 s, (d) Dynamic conditions at t = 8.0 s

Overall, Incremental conductance yields the best multi-metric balance, energy 0.281 Wh (+21.6% vs. PSO; +95.8% vs. P&O), $t_{95} = 3$ ms, hit ratio 62.8%, and the lowest ripple (≈ 41.4 W), placing it near a Pareto-dominant envelope across speed, accuracy, and power quality. Particle Swarm Optimization attains intermediate energy (0.231 Wh) but its convergence penalty ($t_{95} = 206.2$ ms) and re-exploration gaps erode yield during nonstationary intervals despite only moderate ripple. Firefly control is the fastest ($t_{95} = 2.6$ ms) yet unstable, energy 0.094 Wh, hit ratio 10.8%, ripple ≈ 92 W, while P&O remains simple but trap-prone, with lower energy (0.143 Wh) and the highest ripple (≈ 100 W). Distributional evidence aligns with these patterns: INC shows the smallest median/IQR in loss, PSO exhibits heavy tails at regime boundaries, FP the broadest dispersion, and all methods share ~ 220 W transition spikes, confirming that speed alone is insufficient without sustained dwell at the global optimum.

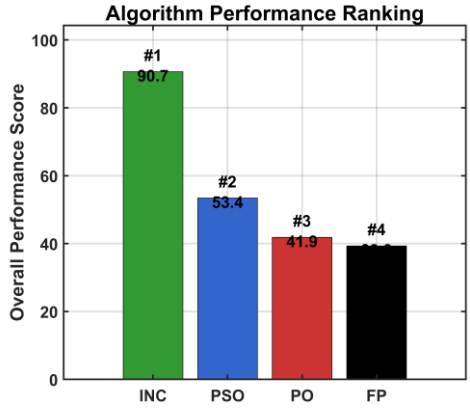

(a)

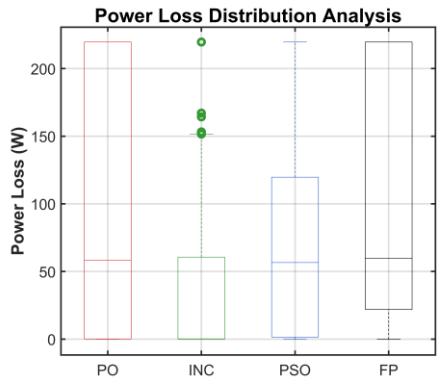

(b)

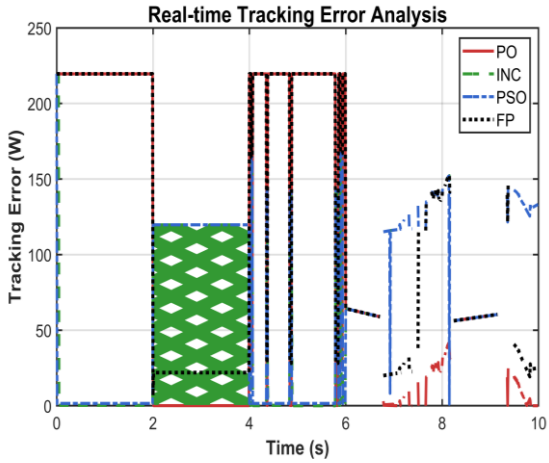

(c)

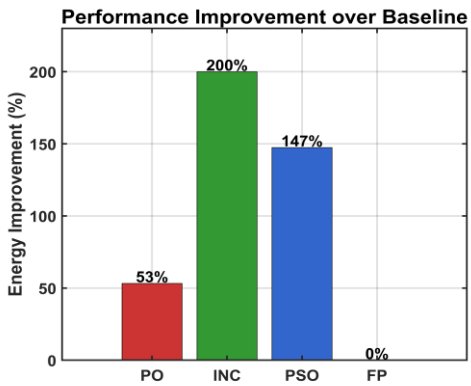

(d)

Figure 5. Statistical performance analysis: (a) Overall algorithm ranking with composite scores, (b) Power loss distribution boxplots, (c) Real-time tracking error dynamics, (d) Energy improvement relative to baseline

5. CONCLUSIONS

This work established a rigorous and reproducible benchmark of four representative MPPT algorithms under dynamic partial shading conditions. The results show a clear and consistent hierarchy in both energy capture and tracking stability. Incremental Conductance (INC) achieved the highest harvested energy of 0.281 Wh, the shortest convergence time of approximately 3.0 ms, the highest GMPP hit ratio of 62.8 % and the lowest power ripple of 41.38 W. These characteristics indicate stable residence near the global maximum power point and robust behaviour under rapidly varying irradiance.

Particle Swarm Optimization (PSO) increased energy extraction compared to Perturb and Observe (P&O) but required a markedly longer convergence time of 206.2 ms and exhibited larger oscillations, reflecting a tradeoff between exploration capability and dynamic stability. Flower Pollination (FP) converged rapidly with a mean time of 2.6 ms, yet its strong global exploration led to frequent departures from the vicinity of the optimum, resulting in the lowest energy yield of 0.094 Wh and the lowest hit ratio of 10.8 %.

The statistical analysis confirmed that these differences are systematic rather than incidental. Kruskal-Wallis testing demonstrated significant separation among the algorithms, while Cliff's delta revealed strong dominance of INC over P&O and FP, and a consistent advantage over PSO across most realizations.

In this study, the MPPT controllers were evaluated at the DC side without explicit modelling of converter or inverter dynamics. As a result, switching effects, control loop bandwidth limits and grid interactions were not represented. Therefore, the present results should be interpreted as an upper bound on achievable MPPT performance and as a comparative ranking of control strategies under ideal power stage behaviour. The low ripple and stable tracking of INC suggest favourable integration in practical systems, whereas more oscillatory methods may impose additional stress on power electronic components. Future work may incorporate detailed converter and grid models to extend the validation toward full system deployment.

ACKNOWLEDGMENT

The author gratefully acknowledges the support of the Thai Nguyen University of Technology and the Education Technology and Adaptive Learning Institute, Thai Nguyen University of Technology, Vietnam.

REFERENCES

[1] Abdulmawjood, K., Alsadi, S., Refaat, S.S., Morsi, W.G. (2022). Characteristic study of solar photovoltaic array under different partial shading conditions. IEEE Access, 10: 6856-6866. http://doi.org/10.1109/ACCESS.2022.3142168

[2] Bhadoria, V.S., Pachauri, R.K., Tiwari, S., Jaiswal, S.P., Alhelou, H.H. (2020). Investigation of different BPD placement topologies for shaded modules in a series-parallel configured PV array. IEEE Access, 8: 216911-216921. http://doi.org/10.1109/ACCESS.2020.3041715

[3] Ahmed, R.M., Zakzouk, N.E., Abdelkader, M.I., Abdelsalam, A.K. (2021). Modified partial-shading-tolerant multi-input-single-output photovoltaic string converter. IEEE Access, 9: 30663-30676. http://doi.org/10.1109/ACCESS.2021.3058695

[4] Bi, Z., Ma, J., Man, K.L., Smith, J.S., Yue, Y., Wen, H. (2020). An enhanced $0.8V_{OC}$-model-based global maximum power point tracking method for photovoltaic systems. IEEE Transactions on Industry Applications, 56(6): 6825-6834. http://doi.org/10.1109/TIA.2020.3019364

[5] Hendy, M.A., Nayel, M.A., Rodriguez, J., Abdelrahem, M. (2024). Enhanced maximum power point tracking using modified PSO hybrid with MPC under partial shading conditions. IEEE Access, 12: 145318-145330. http://doi.org/10.1109/ACCESS.2024.3471829

[6] Pervez, I., Pervez, A., Tariq, M., Sarwar, A., Chakrabortty, R.K., Ryan, M.J. (2020). Rapid and robust adaptive Jaya (Ajaya) based maximum power point tracking of a PV-based generation system. IEEE Access, 9: 48679-48703. http://doi.org/10.1109/ACCESS.2020.3028609

[7] Joisher, M., Singh, D., Taheri, S., Espinoza-Trejo, D.R., Pouresmaeil, E., Taheri, H. (2020). A hybrid evolutionary-based MPPT for photovoltaic systems under partial shading conditions. IEEE Access, 8: 38481-38492. http://doi.org/10.1109/ACCESS.2020.2975742

[8] Alshareef, M.J. (2022). An effective falcon optimization algorithm based MPPT under partial shaded photovoltaic systems. IEEE Access, 10: 131345-131360. http://doi.org/10.1109/ACCESS.2022.3226654

[9] Li, L., Chen, Y., Liu, H., Tang, W., Liu, M., Wu, J., Li, Z. (2020). A multi-producer group-search-optimization method-based maximum-power-point-tracking for uniform and partial shading condition. IEEE Access, 8: 184688-184696. http://doi.org/10.1109/ACCESS.2020.3028934

[10] Liao, C.Y., Subroto, R.K., Millah, I.S., Lian, K.L., Huang, W.T. (2020). An improved bat algorithm for more efficient and faster maximum power point tracking for a photovoltaic system under partial shading conditions. IEEE Access, 8: 96378-96390. http://doi.org/10.1109/ACCESS.2020.2993361

[11] Xu, H., Zhao, M., Xue, F., Zhang, X., Sun, L. (2023). An improved mayfly algorithm with shading detection for MPPT of photovoltaic systems. IEEE Access, 11: 110827-110836. http://doi.org/10.1109/ACCESS.2023.3318129

[12] Chu, G., Wen, H., Yang, Y., Wang, Y. (2019). Elimination of photovoltaic mismatching with improved submodule differential power processing. IEEE Transactions on Industrial Electronics, 67(4): 2822-2833. http://doi.org/10.1109/TIE.2019.2908612

[13] Uno, M., Yamamoto, M., Sato, H., Oyama, S. (2019). Modularized differential power processing architecture based on switched capacitor converter to virtually unify mismatched photovoltaic panel characteristics. IEEE Transactions on Power Electronics, 35(2): 1563-1575. http://doi.org/10.1109/TPEL.2019.2922504

[14] Jeong, H., Park, S., Jung, J.H., Kim, T., Kim, A.R., Kim, K.A. (2020). Segmented differential power processing converter unit and control algorithm for photovoltaic systems. IEEE Transactions on Power Electronics, 36(7): 7797-7809. http://doi.org/10.1109/TPEL.2020.3044417

[15] Alenezi, A., Hussain, H.A. (2023). A new control approach for least processed power tracking under

mismatch conditions in PV systems using differential power processing. IEEE Transactions on Industry Applications, 60(1): 532-543. http://doi.org/10.1109/TIA.2023.3312651

[16] Badawy, M.O., Bose, S.M., Sozer, Y. (2020). A novel differential power processing architecture for a partially shaded PV string using distributed control. IEEE Transactions on Industry Applications, 57(2): 1725-1735. http://doi.org/10.1109/TIA.2020.3046430

[17] Wang, X., Wen, H., Chu, G., Zhu, Y., Yang, Y., Wang, Y., Jiang, L. (2023). Performance quantization and comparative assessment of voltage equalizers in mismatched photovoltaic differential power processing systems. IEEE Transactions on Power Electronics, 39(1): 1656-1675. http://doi.org/10.1109/TPEL.2023.3328325

[18] Shams, I., Mekhilef, S., Tey, K.S. (2022). Extendable voltage equalizer topology with reduced switch count and MPPT with partial shading detection capability for long serially connected PV modules. IEEE Transactions on Industry Applications, 58(5): 6459-6470. http://doi.org/10.1109/TIA.2022.3182644

[19] Xu, C., Itako, K., Kudoh, T., Koh, K., Ge, Q. (2021). Proposal for an active PV array to improve system efficiency during partial shading. IEEE Access, 9: 143423-143433. http://doi.org/10.1109/ACCESS.2021.3121700

[20] Jalal, M., Khalil, I.U., Haq, A.U., Flah, A., Wahab, S.A.M.A. (2024). Advancements in PV array reconfiguration techniques. IEEE Access, 12: 183751-183778. http://doi.org/10.1109/ACCESS.2024.3509955

[21] Madhanmohan, V.P., Saleem, A., Nandakumar, M. (2020). An algorithm for enhanced performance of photovoltaic array under partial shading condition. IEEE Access, 8: 176947-176959. http://doi.org/10.1109/ACCESS.2020.3025906

[22] Kumar, B.P., Cherukuri, S.K., Kaniganti, K.R., Karuppiah, N., Muniraj, R., Babu, T.S., Alhelou, H.H. (2021). Performance enhancement of partial shaded photovoltaic system with the novel screw pattern array configuration scheme. IEEE Access, 10: 1731-1744. http://doi.org/10.1109/ACCESS.2021.3138917

[23] Kermadi, M., Salam, Z., Ahmed, J., Berkouk, E.M. (2020). A high-performance global maximum power point tracker of PV system for rapidly changing partial shading conditions. IEEE Transactions on Industrial Electronics, 68(3): 2236-2245. http://doi.org/10.1109/TIE.2020.2972456

[24] Daryaei, M., Esteki, M., Khajehoddin, S.A. (2023). High efficiency and full MPPT range partial power processing PV module-integrated converter. IEEE Transactions on Power Electronics, 38(5): 6627-6641. http://doi.org/10.1109/TPEL.2023.3243174

[25] Uno, M., Liu, X., Sato, H., Saito, Y. (2022). Panel-to-Substring PWM differential power processing converter and its maximum power point tracking technique for solar roof of plug-in electric vehicles. IEEE Access, 10: 42883-42896. http://doi.org/10.1109/ACCESS.2022.3168583

[26] Mahmud, S., Collings, W., Barchowsky, A., Javaid, A.Y., Khanna, R. (2022). Global maximum power point tracking in dynamic partial shading conditions using ripple correlation control. IEEE Transactions on Industry Applications, 59(2): 2030-2040. http://doi.org/10.1109/TIA.2022.3228227

[27] Anh, T.V., Trieu, T.N., Nghi, P.V.H., Van Hien, B. (2024). Fast and accurate GMPPT based on modified P&O algorithm. IEEE Access, 12: 129588-129600. http://doi.org/10.1109/ACCESS.2024.3457825

[28] Kumar, P., Kumar, M., Bansal, A.K. (2023). GMPP tracking of solar PV system using spotted hyena and quadratic approximation based hybrid algorithm under partially shaded conditions. IEEE Access, 13: 121762-121771. http://doi.org/10.1109/ACCESS.2023.3272554

[29] Khan, H., Sher, H.A., Hussain, A., Noman, A.M., Murtaza, A.F., AboRas, K.M. (2024). Improved RCC-based MPPT strategy for enhanced solar energy harvesting in shaded environments. IEEE Access, 12: 111035-111044. http://doi.org/10.1109/ACCESS.2024.3440841

[30] Guo, K., Cui, L., Mao, M., Zhou, L., Zhang, Q. (2020). An improved gray wolf optimizer MPPT algorithm for PV system with BFBIC converter under partial shading. IEEE Access, 8: 103476-103490. http://doi.org/10.1109/ACCESS.2020.2999311

[31] Pervez, I., Antoniadis, C., Ghazzai, H., Massoud, Y. (2023). A modified bat algorithm with reduced search space exploration for MPPT under dynamic partial shading conditions. In 2023 IEEE International Symposium on Circuits and Systems (ISCAS), Monterey, CA, USA, pp. 1-5. https://doi.org/10.1109/ISCAS46773.2023.10181763

[32] Allahabadi, S., Iman-Eini, H., Farhangi, S. (2021). Fast artificial neural network based method for estimation of the global maximum power point in photovoltaic systems. IEEE Transactions on Industrial Electronics, 69(6): 5879-5888. http://doi.org/10.1109/TIE.2021.3094463

[33] Song, G., Liu, X., Tian, J., Xiao, G., Zhao, T., Wang, P. (2023). Global maximum power point tracking for PV conversion systems under partial shadings: NNIDA based approach. IEEE Transactions on Power Delivery, 38(5): 3179-3191. http://doi.org/10.1109/TPWRD.2023.3271153

[34] Zhu, Y., Yang, Y. (2023). High-performance global maximum power point tracking for partial shaded photovoltaic systems. In 2023 IEEE 14th International Symposium on Power Electronics for Distributed Generation Systems (PEDG), Shanghai, China, pp. 1137-1142. https://doi.org/10.1109/PEDG56097.2023.10215238

[35] Tafti, H.D., Wang, Q., Townsend, C.D., Pou, J., Konstantinou, G. (2022). Global flexible power point tracking in photovoltaic systems under partial shading conditions. IEEE Transactions on Power Electronics, 37(9): 11332-11341. http://doi.org/10.1109/TPEL.2022.3167657

[36] Sakthivel, S.S., Arunachalam, V. (2024). Improved global maximum power point tracking technique for a partially shaded solar photovoltaic array using capacitor transient effect. IEEE Transactions on Industrial Informatics, 20(12): 13853-13862. http://doi.org/10.1109/TII.2024.3435511

[37] Ahmed, S., Mekhilef, S., Mubin, M., Tey, K.S., Kermadi, M. (2023). An adaptive perturb and observe algorithm with enhanced skipping feature for fast global maximum power point tracking under partial shading conditions. IEEE Transactions on Power Electronics, 38(9): 11601-11613. http://doi.org/10.1109/TPEL.2023.3285243

[38] Yang, F., Wu, H., Li, X., Gao, Z., Alkanderi, M. (2023).

Optimized maximum power point tracking for PV system under partial shading conditions. In 2023 IEEE 2nd International Power Electronics and Application Symposium (PEAS), Guangzhou, China, pp. 697-703. https://doi.org/10.1109/PEAS58692.2023.10395405

[39] Widyartono, M., Rahmadian, R. (2020). Partial shading effect on IV characteristic and maximum power of a photovoltaic array. In 2020 Third International Conference on Vocational Education and Electrical Engineering (ICVEE), Surabaya, Indonesia, pp. 1-5. https://doi.org/10.1109/ICVEE50212.2020.9243237

[40] Kumaresan, A., Tafti, H.D., Beniwal, N., Gorla, N.B.Y., Farivar, G.G., Pou, J., Konstantinou, G. (2023). Improved secant-based global flexible power point tracking in photovoltaic systems under partial shading conditions. IEEE Transactions on Power Electronics, 38(8): 10383-10395. http://doi.org/10.1109/TPEL.2023.3277580

[41] Shams, I., Mekhilef, S., Tey, K.S. (2020). Improved-team-game-optimization-algorithm-based solar MPPT with fast convergence speed and fast response to load variations. IEEE Transactions on Industrial Electronics, 68(8): 7093-7103. http://doi.org/10.1109/TIE.2020.3001798

[42] Maihulla, A.S., Yusuf, I., Bala, S.I. (2022). Reliability and performance analysis of a series-parallel system using Gumbel–Hougaard family copula. Journal of Computational and Cognitive Engineering, 1(2): 74-82. http://doi.org/10.47852/bonviewJCCE2022010101

[43] Riquelme-Dominguez, J.M., Martinez, S. (2022). Systematic evaluation of photovoltaic MPPT algorithms using state-space models under different dynamic test procedures. IEEE Access, 10: 45772-45783. http://doi.org/10.1109/ACCESS.2022.3170714

[44] Musa, M.A., Yusuf, I., Sanusi, A. (2024). Cost analysis of solar water pumping system for small town water supply. Journal of Computational and Cognitive Engineering, 3(1): 77-86. https://doi.org/10.47852/bonviewJCCE2202212

[45] Kim, C.S., Kim, W., Park, H.P. (2025). DC series arc fault detection capability using auxiliary filter for module-level PV systems. IEEE Access, 13: 39343-39352. https://doi.org/10.1109/ACCESS.2025.3545457

[46] Obukhov, S., Ibrahim, A., Diab, A.A.Z., Al-Sumaiti, A.S., Aboelsaud, R. (2020). Optimal performance of dynamic particle swarm optimization based maximum power trackers for stand-alone PV system under partial shading conditions. IEEE Access, 8: 20770-20785. http://doi.org/10.1109/ACCESS.2020.2966430

[47] Negri, C.A., Daneshvardehnavi, S., Schmitt, K.E.K., Nezhad, A.E., Nardelli, P.H., Bayne, S., Giesselmann, M.G. (2022). Centralized control topology for PV farms shading detection and GMPP searching restarting condition. IEEE Access, 10: 28991-29008. http://doi.org/10.1109/ACCESS.2022.3158739

[48] Basu, T.S., Maiti, S., Chakraborty, C. (2020). Performance improvement of PV-fed hybrid modular multilevel converter under partial shading condition. IEEE Transactions on Industrial Electronics, 68(10): 9652-9664. http://doi.org/10.1109/TIE.2020.3028819

[49] Ahmed, M., Harbi, I., Kennel, R., Rodriguez, J., Abdelrahem, M. (2022). Model-based maximum power point tracking algorithm with constant power generation capability and fast DC-link dynamics for two-stage PV systems. IEEE Access, 10: 48551-48568. http://doi.org/10.1109/ACCESS.2022.3172292

[50] Sharma, S., Varshney, L., Elavarasan, R.M., Vardhan, A.S.S., Vardhan, A.S.S., Saket, R.K., Subramaniam, U., Hossain, E. (2021). Performance enhancement of PV system configurations under partial shading conditions using MS method. IEEE Access, 9: 56630-56644. http://doi.org/10.1109/ACCESS.2021.3071340

[51] Yanarates, C., Wang, Y., Zhou, Z. (2021). Unity proportional gain resonant and gain scheduled proportional (PR-P) controller-based variable perturbation size real-time adaptive perturb and observe (P&O) MPPT algorithm for PV systems. IEEE Access, 9: 138468-138482. http://doi.org/10.1109/ACCESS.2021.3119042

[52] Li, X., Wen, H., Hu, Y., Du, Y., Yang, Y. (2020). A comparative study on photovoltaic MPPT algorithms under EN50530 dynamic test procedure. IEEE Transactions on Power Electronics, 36(4): 4153-4168. http://doi.org/10.1109/TPEL.2020.3024211

[53] Saxena, V., Kumar, N., Singh, B., Panigrahi, B.K. (2020). A rapid circle centre-line concept-based MPPT algorithm for solar photovoltaic energy conversion systems. IEEE Transactions on Circuits and Systems I: Regular Papers, 68(2): 940-949. http://doi.org/10.1109/TCSI.2020.3038114

[54] Shamsmohammadi, N. (2024). Investigating and classifying the level of thermal runaway-induced failure energy storage systems in photovoltaics. Journal of Computational and Cognitive Engineering, 3(1): 15-23. http://doi.org/10.47852/bonviewJCCE32021698

[55] Wang, S.C., Pai, H.Y., Chen, G.J., Liu, Y.H. (2020). A fast and efficient maximum power tracking combining simplified state estimation with adaptive perturb and observe. IEEE Access, 8: 155319-155328. http://doi.org/10.1109/ACCESS.2020.3019197

[56] Kiran, S.R., Basha, C.H., Singh, V.P., Dhanamjayulu, C., Prusty, B.R., Khan, B. (2022). Reduced simulative performance analysis of variable step size ANN based MPPT techniques for partially shaded solar PV systems. IEEE Access, 10: 48875-48889. http://doi.org/10.1109/ACCESS.2022.3172322

[57] Al Ghamri, M., Ibrahim, D., Sihwail, R., Shehab, M. (2025). Whale optimization algorithm for feature selection enhances classification in malware datasets. Journal of Computational and Cognitive Engineering, 4(3), 387-396. http://doi.org/10.47852/bonviewJCCE42024233

[58] Irodov, V., Dubrovskyi, S., Dudkin, K., Chirin, D., Aldrich, Y. (2024). Evolutionary search for stochastic optimization with binary choice relations under fuzzy modeling. Journal of Computational and Cognitive Engineering, 3(4): 412-420. http://doi.org/10.47852/bonviewJCCE42022658

[59] Ravishankar, S., Battineni, G. (2025). A survey on recent advancements in auto-machine learning with a focus on feature engineering. Journal of Computational and Cognitive Engineering, 4(1): 56-63. http://doi.org/10.47852/bonviewJCCE3202720

[60] Zhang, Y., Ping, P., Dai, X., Li, C., Li, Z., Zhuo, P., Tang, L., Kong, D., Yin, X. (2024). Failure mechanism and thermal runaway behavior of lithium-ion battery induced by arc faults. Renewable and Sustainable Energy Reviews, 207: 114914.

http://doi.org//10.1016/j.rser.2024.114914
[61] Yuan, J., Zhao, Z., Liu, Y., He, B., Wang, L., Xie, B., Gao, Y. (2021). DMPPT control of photovoltaic microgrid based on improved sparrow search algorithm. IEEE Access, 9: 16623-16629. http://doi.org/10.1109/ACCESS.2021.3052960
[62] Sai, B.S.V., Chatterjee, D., Mekhilef, S., Wahyudie, A. (2022). An SSM-PSO based MPPT scheme for wind driven DFIG system. IEEE Access, 10: 78306-78319. http://doi.org/10.1109/ACCESS.2022.3193998
[63] Pillai, D.S., Ram, J.P., Ghias, A.M., Mahmud, M.A., Rajasekar, N. (2019). An accurate, shade detection-based hybrid maximum power point tracking approach for PV systems. IEEE Transactions on Power Electronics, 35(6): 6594-6608. http://doi.org/10.1109/TPEL.2019.2953242
[64] Manoharan, P., Subramaniam, U., Babu, T.S., Padmanaban, S., Holm-Nielsen, J.B., Mitolo, M., Ravichandran, S. (2020). Improved perturb and observation maximum power point tracking technique for solar photovoltaic power generation systems. IEEE Systems Journal, 15(2): 3024-3035. http://doi.org/10.1109/JSYST.2020.3003255
[65] Kumar, M., Panda, K.P., Rosas-Caro, J.C., Valderrabano-Gonzalez, A., Panda, G. (2023). Comprehensive review of conventional and emerging maximum power point tracking algorithms for uniformly and partially shaded solar photovoltaic systems. IEEE Access, 11: 31778-31812. http://doi.org/10.1109/ACCESS.2023.3262502
[66] Chuku, A.J., Adumene, S., Orji, C.U., Johnson, K.T., Nitonye, S. (2023). Dynamic failure analysis of ship energy systems using an adaptive machine learning formalism. Journal of Computational and Cognitive Engineering, 2(4): 312-321. http://doi.org/10.47852/bonviewJCCE3202491
[67] Ayaz, R. (2024). Self-tuning parameters of the proposed fuzzy immune integral controller to improve the performance of the standard P&O-MPPT strategy. IEEE Access, 12: 192396-192414. http://doi.org/10.1109/ACCESS.2024.3519495
[68] Ibrahim, A.W., Fang, Z., Li, R., Zhang, W., et al. (2024). Intelligent nonlinear PID-Controller combined with optimization algorithm for effective global maximum power point tracking of PV systems. IEEE Access, 12: 185265-185290. http://doi.org/10.1109/ACCESS.2024.3513355
[69] Yilmaz, M., Celikel, R., Gundogdu, A. (2023). Enhanced photovoltaic systems performance: Anti-windup PI controller in ANN-based ARV MPPT method. IEEE Access, 11: 90498-90509. http://doi.org/10.1109/ACCESS.2023.3290316